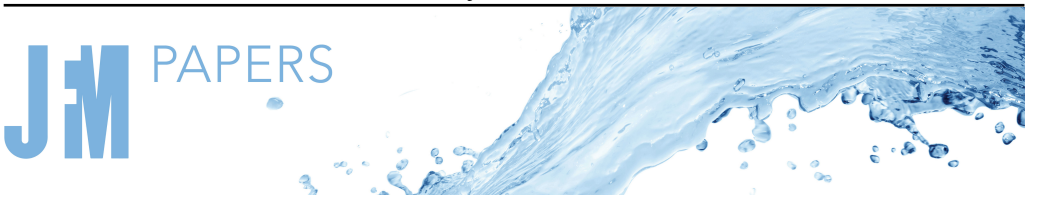
J. Fluid Mech. (2025), *vol.* 1025, A36, doi:10.1017/jfm.2025.10933



Nonlinear dynamics analysis of an ionic surfactant-laden thread in a radial electric field

Xiaocong Yang[1], **Jun Gao**[1], **Hu Sun**[1], **Qiyou Liu**[1], **Wentong Qiao**[1], **Bingqiang Ji**[1], **Dongdong He**[2] **and Qingfei Fu**[1]

[1]School of Astronautics, Beihang University, Beijng 100191, PR China

[2]School of Science and Engineering, The Chinese University of Hong Kong (Shenzhen), Longgang, Shenzhen, Guangdong 518172, PR China

Corresponding authors: Dongdong He, hedongdong@cuhk.edu.cn; Qingfei Fu, fuqingfei@buaa.edu.cn

(Received 7 November 2024; revised 22 August 2025; accepted 6 November 2025)

Ionic surfactants are commonly employed to modify the rheological properties of fluids, particularly in terms of surface viscoelasticity. Concurrently, external electric fields can significantly impact the dynamics of liquid threads. A key question is how ionic surfactants affect the dynamic behaviour of threads in the presence of an electric field? To investigate this, a one-dimensional model of a liquid thread coated with surfactants within a radial electric field is established, employing the long-wave approximation. We systematically investigate the effects of dimensionless parameters associated with the surfactants, including surfactant concentration, dilatational Boussinesq number $Bo_{\kappa\infty}$ and shear Boussinesq number $Bo_{\mu\infty}$. The results indicate that increasing the surfactant concentration and the two Boussinesq numbers reduces both the maximum growth rate and the dominant wavenumber. In addition, both the electric field and surfactants mitigate the breakup of the liquid thread and the formation of satellite droplets. At low applied electric potentials, the surface viscosity induced by surfactants predominantly governs this suppression. Surface viscosity suppresses the formation of satellite droplets by maintaining the neck point at the centre of the liquid thread within a single disturbance wavelength. When the applied potential is high, the electric stress has two main effects: the external electric field exerts a normal pressure on the liquid thread surface, suppressing satellite droplet formation, while the internal electric field inhibits liquid drainage. Surface viscosity further stabilizes the system by suppressing flow dynamics during this process.

Key words: slender-body theory, nonlinear instability

1. Introduction

Electrically charged threads hold significant application value in processes such as electrospraying, microfluidics, chemical processing, pharmaceuticals and rheometry.

© The Author(s), 2025. Published by Cambridge University Press.

https://doi.org/10.1017/jfm.2025.10933 Published online by Cambridge University Press

They are already widely utilized in inkjet printing and electrospinning, as electric fields can facilitate the generation of uniformly sized droplets and suppress drainage induced by capillary forces (Sweet 1965; Reneker *et al.* 2000; Hohman *et al.* 2001*b*; Ismail *et al.* 2016; Wang *et al.* 2018). The coupling of electric and flow fields has resulted in new phenomena related to jet instability and breakup, and exploring the underlying mechanisms undoubtedly enriches the foundations of electrokinetics and electrohydrodynamics.

Research on electrically charged jets typically involves the application of either axial or radial electric fields. In the case of axial fields, linear stability analyses of both uncharged and charged jets (Mestel 1996; Saville 1971*a*) demonstrate that electric fields exert a stabilizing influence, thereby facilitating the formation of exceptionally long fibres. Hohman investigated the instability of charged viscous jets in axisymmetric and 'whipping' modes (Hohman *et al.* 2001*a*,*b*). Regarding radial electric fields, Huebner & Chu (1971) conducted a linear stability analysis of perfectly conducting jets, discovering that finite disturbances are stable under long-wave conditions and unstable under short-wave conditions. Saville (1971*b*) explored the linear stability of concentric electrodes placed at an infinite distance, while Collins, Harris & Basaran (2007) examined the effects of incompatible surfaces on cylindrical electrodes at finite distances. Saville (1997) employed the Taylor–Melcher leaky-dielectric model to study the stability of three-dimensional dielectric fluids, while López-Herrera *et al.* (2005) investigated scenarios devoid of electric effects. López-Herrera & Gañán-Calvo (2004) provided numerical solutions for perfectly conducting Newtonian fluids under radial electric fields using a one-dimensional model. Collins *et al.* (2007) explored both one-dimensional and two-dimensional models, demonstrating that electric stress significantly increases the size of satellite droplets. Additionally, Wang, Mählmann & Papageorgiou (2009) utilized a similar model to study the evolution of jets, simulating the axisymmetric nonlinear dynamics of perfectly conducting viscous liquid jets under radial electric fields. Furthermore, Conroy *et al.* (2010) investigated the rupture of electrolyte annular liquid threads under the influence of electrostatic and electric effects in radial electric fields over finite time scales. López-Herrera & Gañán-Calvo (2004) conducted experimental studies to examine the effects of viscosity and electric field strength on the size and charge of satellite droplets in perfectly conducting jets under radial electric fields. They compared their experimental results with predictions from a one-dimensional model, achieving good agreement at moderate to low electric field strengths.

Collins *et al.* (2007) developed a robust Galerkin finite-element algorithm to solve the two-dimensional Navier–Stokes equations alongside the Laplace equation. This model controlled the axisymmetric deformation and breakup of a perfectly conducting, incompressible Newtonian fluid under a radial electric field. In another work, Wang & Papageorgiou (2011) studied the axisymmetric breakup of a perfectly conducting viscous liquid thread immersed in another viscous fluid using boundary integral methods, focusing on the zero Reynolds number limit. Their research highlighted the role of electric stress in stabilizing or destabilizing the liquid thread. Additionally, Wang (2012) extended this work to analyse poorly conducting Stokes jets suspended in a viscous medium. This study revealed that the formation of satellite droplets differs significantly from the perfectly conducting case, suggesting that electric shear stress promotes the formation of multiple satellite droplets. López-Herrera *et al.* (2015) simulated the breakup of charged liquid jets, taking into account the time scales associated with diffusion and electro-osmotic migration. Lakdawala, Sharma & Thaokar (2016) introduced a dual-grid level-set method to numerically investigate the nonlinear breakup dynamics of perfectly conducting Newtonian viscous liquid jets under a radial electric field. Li *et al.* (2019) discussed

https://doi.org/10.1017/jfm.2025.10933 Published online by Cambridge University Press

the influence of finite conductivity on the nonlinear dynamics of viscoelastic, weakly conducting liquid jets, concluding that tangential stress prevent the formation of satellite droplets in bead-on-string structures. Finally, Montanero & Ganan-Calvo (2020) provided a comprehensive review of the breakup and stability analysis of charged jets, covering various experimental and theoretical developments in the field.

It has long been recognized that the presence of surfactant molecules can alter the dynamics of fluid interfaces, with numerous applications in various fields (Rodríguez-Rodríguez *et al.* 2015). This influence leads to phenomena such as highly deformed drops in shear or extensional flows (Eggers 1997; Anna 2016; Montanero & Ganan-Calvo 2020), as well as the formation of flower-like patterns due to the evaporation of droplets on a liquid substrate (Wodlei *et al.* 2018). In recent years, surfactants have become one of the most compelling and widely studied factors in problems involving liquid–air and liquid–liquid interfaces. However, the underlying mechanisms remain only partially understood.

Surfactants at liquid surfaces can influence fluid dynamics through three primary mechanisms (Kamat *et al.* 2018; Montanero & Ganan-Calvo 2020; Wee, Wagoner & Basaran 2022). First, the solutocapillary effect, which reduces capillary forces by lowering the surface tension coefficient. Second, the Marangoni effect, caused by an uneven distribution of surfactants along the interface, resulting in surface tension gradients. Last, surfactants induce surface rheological effects, characterized by surface shear viscosity and surface dilatational viscosity, generating additional viscous stresses.

The investigation of how factors such as capillarity, bulk viscosity, inertia, Marangoni stress and surface viscosity compete or cooperate in fluid systems is of both scientific and practical significance. Experiments and theoretical studies have demonstrated that surface viscosity plays a crucial role in various interfacial flows, such as foams (Joye, Hirasaki & Miller 1994), liquid threads (Scheid *et al.* 2010), liquid bridges (Ponce-Torres *et al.* 2016*a*,*b*) and droplet breakup (Ponce-Torres *et al.* 2017). Specifically, Ponce-Torres *et al.* (Ponce-Torres *et al.* 2017) concluded that surface viscosity determines the amount of surfactant retained in satellite droplets formed after pinch-off. Similarly, the effects of surface elasticity induced by the presence of surfactants have been explored in several configurations, including liquid threads (Craster, Matar & Papageorgiou 2002; Timmermans & Lister 2002), dip coating (Campana *et al.* 2011; Seiwert, Dollet & Cantat 2014; Champougny *et al.* 2015), bubbles immersed in a viscous medium (Hameed *et al.* 2008) and droplet deformation and breakup (Stone & Leal 1990; Milliken, Stone & Leal 1993).

The linear theory has confirmed that the presence of surfactants exerts a stabilizing effect on the Rayleigh–Plateau instability of Newtonian viscous jets (Craster *et al.* 2002; Ponce-Torres *et al.* 2016*a*; Martínez-Calvo & Sevilla 2018). This stabilizing effect manifests through a reduction in the growth rate of small perturbations, as surfactants lower the mean capillary force while introducing Marangoni stress and surface viscous stresses. Correspondingly, increasing surfactant activity or surface viscosity enhances jet stability. However, linear analysis based on the long-wave approximation cannot accurately predict certain instability characteristics, such as the cutoff wavenumber, for surfactant-laden jets and filaments without incorporating necessary higher-order terms (Timmermans & Lister 2002; Martínez-Calvo & Sevilla 2018).

Nonetheless, linear theory cannot capture the later stages of jet or filament instability. The nonlinear dynamics of Newtonian jets and filaments in the presence of surfactants have been extensively studied using asymptotic methods and numerical simulations (Craster *et al.* 2002; Timmermans & Lister 2002; Dravid *et al.* 2006; McGough & Basaran 2006; Craster, Matar & Papageorgiou 2009; Hameed & Maldarelli 2016; Martínez-Calvo *et al.* 2020; Wee *et al.* 2021). These studies revealed that surfactants can delay

https://doi.org/10.1017/jfm.2025.10933 Published online by Cambridge University Press

the retraction of Newtonian liquid filaments (Craster *et al.* 2002). The presence of surfactants affects the formation of satellite droplets between primary droplets, with the size of the satellite droplets increasing or decreasing depending on surfactant strength and diffusivity. Experiments and simulations by McGough & Basaran (2006) and Kamat *et al.* (2018) showed that Marangoni stress near the pinching point leads to the formation of microthread cascades. When the transport of insoluble surfactants is dominated by surface convection (i.e. at high surface Péclet numbers), surfactant molecules are swept away from the pinching point (the neck of the liquid filament between primary droplets), making the behaviour of surfactant-laden jets prior to breakup similar to that of clean jets (McGough & Basaran 2006; Eggers & Villermaux 2008). However, even as most surfactant molecules are swept away, surface viscous stresses can still play a role because the surface-to-volume ratio at the pinching point becomes very large as the minimum jet radius approaches zero (Martínez-Calvo *et al.* 2020; Wee *et al.* 2021). Moreover, surfactant molecules are not always entirely expelled from the pinching point, even at Péclet numbers as high as 10^5 (Ponce-Torres *et al.* 2020).

Nonlinear analysis of one-dimensional models of surfactant-laden viscous filaments in the Stokes regime reveals the existence of a critical surface Péclet number. Below this critical value, surface diffusion dominates, and the filament thins exponentially over time; above this value, surface convection becomes dominant, and the thinning exhibits a time-dependent power-law behaviour until breakup (Wee *et al.* 2022). In the Stokes limit, surface viscous stresses enter the primary force balance and tend to slow the thinning of Newtonian filaments (Ozan & Jakobsen 2019; Wee *et al.* 2020). At sufficiently high surfactant surface concentrations, the balance between capillary forces and surface viscous stresses leads to exponential thinning in time, with the rate dependent solely on surface tension and surface viscosity (Martínez-Calvo & Sevilla 2020). When inertia is considered, near the jet's breakup point, a dominant force balance is established among inertia, capillary forces, bulk viscosity and surface viscosity, while Marangoni stress plays a secondary role (Wee *et al.* 2021). Studies of surfactant effects have also been extended to compound liquid jets (Yao, Yang & Fu 2021).

However, it is important to note that, despite many surfactants being ionic and thus influenced by electric fields, and their applications in electrohydrodynamic spraying, research on electrically driven jets containing surfactants remains relatively limited. Gallardo *et al.* (1999) demonstrated the use of charged surfactants to manipulate small droplets by applying an electric field. Electrified surfactants exhibit two primary effects: first, they alter surface tension; second, they influence the surface potential of the system. The surface tension results from a combination of the usual Langmuir adsorption isotherm and electrostatic contributions (Prosser & Franses 2001; Baygents & Saville 1991). In addition, charged surfactants affect both the fluid's bulk potential and the interfacial potential, which can be represented through the Maxwell stress tensor, as studied by Conroy *et al.* (2010, 2011). However, no prior research has explored the combined effects of electric forces and surface viscosity in liquid thread with charged surfactants, although surface viscosity is crucial for the dynamic analysis of liquid thread containing surfactants. This interaction introduces novel dynamical behaviours that have yet to be analysed. Therefore, in this paper, ionic surfactants and their associated surface viscosity are considered, employing the Boussinesq–Scriven model. The governing equations are non-dimensionalized and simplified under the long-wave approximation, leading to a one-dimensional model. Numerical simulations are performed to investigate the dynamics of the system.

The remainder of this paper is organized as follows. In § 2, we describe the physical model and governing equations, followed by the derivation of the simplified

https://doi.org/10.1017/jfm.2025.10933 Published online by Cambridge University Press

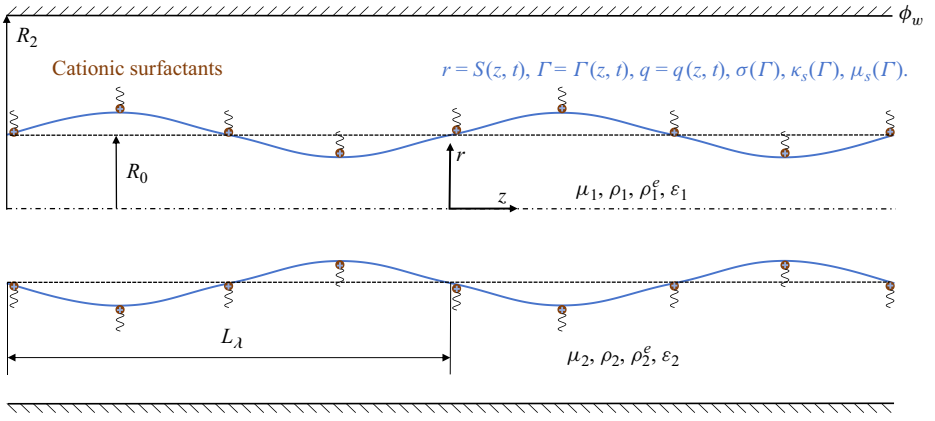


Figure 1. Schematic diagram of a liquid thread enveloped in a radial electric field containing ionic surfactants.

one-dimensional model. In § 3, we perform a linear stability analysis and present the results. Section 5 outlines the numerical methods and results. Finally, conclusions are provided in § 6.

2. Model

Consider an infinitely long axisymmetric liquid thread, surrounded by air, as depicted in figure 1. It should be noted that, in any given real-world system of charged jets, the applied electric field usually contains both radial and axial components, and the precise strength of each individual component is difficult to measure (Lakdawala *et al.* 2016). Consequently, theoretical and numerical studies usually focus on one component of the electric field, either radial or axial. As the radial electric field is essential for elucidating the breakup modes of liquid threads and the formation of satellite droplets (Nie *et al.* 2021), in this study, an axisymmetric radial electric field is present outside the liquid thread, which generated by a cylindrical electrode with a radius R_2 and a uniform wall potential ϕ_w at R_2. Prior to perturbation, the liquid thread is stationary with no underlying flow and a radius R_0. The rheological properties, including dilatational surface viscosity and shear surface viscosity induced by surfactants, are considered. For flows with high viscosity, low velocity and small characteristic thickness, the bond number quantifying the ratio of gravity and inertia is very small, and the influence of aerodynamic forces is weak. Therefore, the hydrodynamic effects of air and gravity are neglected. An axisymmetric coordinate system (r, z) is established, where r represents the radial direction and z represents the axial direction. Upon an axisymmetric harmonic perturbation being imposed, the thread starts to deform, whose radius is a function of z and time t, denoted by $r = S(z, t)$.

Ionic surfactants are dissolved into the liquid thread and adsorped into the interface. The surface of the liquid thread is covered with the positively charged ionic surfactant of concentration Γ, and the surface electric charge density is q. Regarding the solubility of surfactants, Datwani & Stebe (1999) describes three adsorption dynamics models, among which the diffusion-controlled adsorption model is predominant under diffusion-dominated conditions, yielding the Davies adsorption isotherm at equilibrium. This study adopts the diffusion-controlled adsorption model, positing that ionic surfactants dissolve in liquid and immediately diffuse to the surface, with the characteristic time for adsorption being much shorter than the characteristic time for diffusion, and the diffusion characteristic time being significantly shorter than the characteristic time for

https://doi.org/10.1017/jfm.2025.10933 Published online by Cambridge University Press

convection. This implies a relatively small Péclet number, which is taken into account when simplifying the model in this study. In addition, the cylindrical liquid thread is a dielectric with viscosity μ_1, density ρ_1 and permittivity ε_1, while the air has density ρ_2, viscosity μ_2 and permittivity ε_2. The dielectric constants of the air–water system are approximately $\varepsilon_2/\varepsilon_1 = 1/80$. In the subsequent model, the subscript $'1'$ denotes the liquid thread, and subscript $'2'$ denotes the air.

2.1. *Governing equations*

First, the electrostatic effects are governed by the Maxwell equations in the absence of magnetic fields,

$$\nabla \cdot (\varepsilon_i \boldsymbol{E}_i) = \rho_i^e, \quad \nabla \times \boldsymbol{E}_i = 0, \quad i = 1, 2, \tag{2.1}$$

where ρ_i^e is the volume charge density within the fluid, and $\boldsymbol{E}_i$ is the electric field. We then introduce the electric potential ϕ_i as follows:

$$\boldsymbol{E}_i = -\nabla \phi_i. \tag{2.2}$$

At the interface, electric potential must satisfy the following jump condition:

$$\|\varepsilon \nabla \phi_i \cdot \boldsymbol{n}\| = -q, \quad \|\nabla \phi_i \cdot \boldsymbol{t}\| = 0, \tag{2.3}$$

where q represents the surface charge density. The vectors $\boldsymbol{n}$ and $\boldsymbol{t}$ denote the unit normal (pointing outward) and unit tangential vectors, respectively. The notation $\|(\cdot)\|$ represents the jump of the physical quantity $(\cdot)$ across the interface, defined as $(\cdot)_2 - (\cdot)_1$.

The electrolyte used to induce the ionic surfactant is a symmetric $z:z$ electrolyte. We use superscripts '+' and '−' to denote the positive and negative ions in the core flow, respectively. The concentration of positive and negative ions coming from the dissolution of surfactant in the liquid thread are represented by $c^{(+)}$ and $c^{(-)}$, and the positive charge ions are adsorped into the interface and act as the surfactant, while $n^{(+)}$ and $n^{(-)}$ denote the ions of other electrolytes unaffected by the surfactant. The units of $c^{(\pm)}$ and $n^{(\pm)}$ are in molar concentration. The volume charge density in the core flow can then be expressed as

$$\rho_1^e = eN_A\big(n^{(+)} + c^{(+)} - n^{(-)} - c^{(-)}\big), \tag{2.4}$$

where e is the charge on an electron, and N_A is Avogadro's number. And it is assumed that there is no charge in the air, i.e. $\rho_2^e = 0$.

The surface charge density is given by

$$q = eN_A\big(\Gamma + n_s^{(+)} - n_s^{(-)}\big), \tag{2.5}$$

where Γ represents the positively charged ionic surfactant concentration at the surface. And the surface species n_s^+, n_s^- from other electrolytes satisfy the Nernst–Plank equation at the interface and their maximum electrolyte packing concentration is assumed to be n_s^0 (see (8), (9) and related discussion in Conroy *et al.* (2011)).

The ion concentration in the core flow evolves according to the Nernst–Planck equation,

$$\frac{\mathrm{D}c^{(\pm)}}{\mathrm{D}t} = \nabla \cdot \omega\big[ec^{(\pm)}\nabla\phi_i + k_B T \nabla c^{(\pm)}\big], \quad \frac{\mathrm{D}n^{(\pm)}}{\mathrm{D}t} = \nabla \cdot \omega\big[en^{(\pm)}\nabla\phi_i + k_B T \nabla n^{(\pm)}\big], \tag{2.6}$$

where k_B is the Boltzmann constant, T is the absolute temperature, ω represents the mobility of the species, $\mathrm{D}/\mathrm{D}t$ is the material derivative. Due to considering surfactants and other electrolytes as strong electrolytes, there are no dissociation and association terms for

https://doi.org/10.1017/jfm.2025.10933 Published online by Cambridge University Press

ions in (2.6). In addition, the equilibrium condition in the thread satisfies where the electric potential $\phi_1 = \phi^0$ (assuming $\phi^0 = 0$) and the corresponding total positive and negative ion concentrations are both c_0.

At the interface, the concentration Γ of the positively charged surfactants evolves according to the following evolution equation:

$$\frac{\partial \Gamma}{\partial t} - \frac{\partial \boldsymbol{X}}{\partial t}\nabla_s \Gamma + \nabla_s \cdot (\Gamma \boldsymbol{u}_t) + \Gamma \zeta \boldsymbol{u} \cdot \boldsymbol{n} = \nabla_s \cdot (D_s \nabla_s \Gamma + D_{s\phi} \Gamma \nabla_s \phi_s), \tag{2.7}$$

where $\partial \Gamma / \partial t$ is the time derivative following the evolution of the surface point by keeping the surface coordinates fixed, $\boldsymbol{X}$ is the position vector of the surface point, $\nabla_s = (\boldsymbol{I} - \boldsymbol{nn}) \cdot \nabla$ is the surface gradient operator, $\boldsymbol{u}$ is the velocity of the surface point and $\boldsymbol{u}_t$ is the tangential component of velocity for the corresponding surface point, $\zeta = \nabla \cdot \boldsymbol{n}$ is the curvature at the interface, D_s is the surface diffusion coefficient, $D_{s\phi} = D_s e / k_B T$ is the diffusion coefficient for ion migration and ϕ_s is the electric potential at the interface. The above evolution equation is based on the book chapter (Papageorgiu 2002), where the ion electromigration term is obtained by assuming $J_\phi \; D_{s\phi} \nabla_s \phi_s$. And here we make the equilibrium assumption for low concentrations and ignore surface flux to the interface from the bulk fluid (Conroy *et al.* 2011). This study considers the case where the surfactant concentration does not reach the critical micelle concentration.

The continuity equation and Navier–Stokes equations for the fluid can be written as follows:

$$\nabla \cdot \boldsymbol{u}_i = 0, \quad i = 1, 2, \tag{2.8}$$

$$\rho_i \frac{\mathrm{D}\boldsymbol{u}_i}{\mathrm{D}t} = \nabla \cdot \left(\boldsymbol{T}_i^f + \boldsymbol{T}_i^e\right), \quad i = 1, 2. \tag{2.9}$$

Assuming the fluid is incompressible, the fluid stress tensor and Maxwell stress tensor appearing in (2.9) can be given as follows:

$$\boldsymbol{T}_i^f = -p_i \boldsymbol{I} + \boldsymbol{\tau}_i, \tag{2.10}$$

$$\boldsymbol{T}_i^e = \varepsilon_i \left(\boldsymbol{E}_i \boldsymbol{E}_i - \frac{1}{2}|\boldsymbol{E}_i|^2 \boldsymbol{I}\right). \tag{2.11}$$

Here, p_1 is pressure of the liquid thread, p_2 is air pressure, $\boldsymbol{\tau}_i = \mu_i[\nabla \boldsymbol{u}_i + (\boldsymbol{u}_i)^{\mathrm{T}}]$ and $\nabla \cdot T_i^e = \rho_i^e \boldsymbol{E}_i$.

The boundary conditions can be summarized as kinematic boundary conditions and dynamic boundary conditions. The first is the no-slip boundary condition, with $\boldsymbol{u}_2(R_2, z, t) = \boldsymbol{0}$ at the pipe wall. In addition, there is a continuity of velocity at the gas–liquid interface,

$$\|\boldsymbol{u}_i\| = 0, \tag{2.12}$$

where $\boldsymbol{u}_i = (u_i, w_i)^T$, w_i represents the axial velocity (z direction) and u_i represents the radial velocity (r direction).

The movement of the position of the gas–liquid interface conforms to the kinematic boundary conditions,

$$u_i = S_t + w_i S_z, \tag{2.13}$$

where the velocity term is calculated at the interface. S_t denotes the partial derivative of S with respect to time and S_z denotes the partial derivative of S with respect to z.

In this model, it is assumed that surfactants induce both surface elasticity and surface viscosity at the gas–liquid interface. In other words, it not only reduces surface tension

https://doi.org/10.1017/jfm.2025.10933 Published online by Cambridge University Press

but also causes additional viscous stresses at the interface, as described by Martínez-Calvo & Sevilla (2018). The free-surface stress is simulated by two surface viscosities: surface shear viscosity $\mu_s(\Gamma)$ and dilatational viscosity $\kappa_s(\Gamma)$. Following the derivation process of Martinez-Calvo & Sevilla (2018), the stress balance at the gas–liquid interface can be expressed as follows:

$$\left\| \boldsymbol{T}_i^f + \boldsymbol{T}_i^e \right\| \cdot \boldsymbol{n} + \nabla_s \cdot \boldsymbol{T}_s = 0, \tag{2.14}$$

where the surface stress tensor $\boldsymbol{T}_s$ is defined using the well-known Boussinesq–Scriven approximation, which neglects surface density and simplifies the complex interfacial rheology. This approximation assumes that the deviatoric components of $\boldsymbol{T}_s$ are isotropic, linear and instantaneous in the surface strain rate tensor (Boussinesq 1913; Scriven & Sternling 1960),

$$\boldsymbol{T}_s = \boldsymbol{I}_s[\sigma + (\kappa_s - \mu_s)(\nabla_s \cdot \boldsymbol{u}_s)] + \mu_s \left[(\nabla_s \boldsymbol{u}_s) \cdot \boldsymbol{I}_s + \boldsymbol{I}_s (\nabla_s \boldsymbol{u}_s)^{\mathrm{T}} \right]. \tag{2.15}$$

Substituting the (2.15) into (2.14) yields

$$\begin{aligned} &\left\| \boldsymbol{T}_i^f + \boldsymbol{T}_i^e \right\| \cdot \boldsymbol{n} + \nabla_s \sigma - \boldsymbol{n}(\nabla_s \cdot \boldsymbol{n})\sigma + \nabla_s[(\kappa_s - \mu_s)(\nabla_s \cdot \boldsymbol{u}_s)] \\ &\quad - \boldsymbol{n}(\nabla_s \cdot \boldsymbol{n})(\kappa_s - \mu_s)(\nabla_s \cdot \boldsymbol{u}_s) + \nabla_s \cdot \left\{ \mu_s \left[(\nabla_s \boldsymbol{u}_s) \cdot \boldsymbol{I}_s + \boldsymbol{I}_s \cdot (\nabla_s \boldsymbol{u}_s)^{\mathrm{T}} \right] \right\} = 0, \end{aligned} \tag{2.16}$$

where $\zeta = \nabla_s \cdot \boldsymbol{n} = 1/S\sqrt{1 + S_z^2} - S_{zz}/\sqrt{(1 + S_z^2)^3}$ is mean curvature of the interface.

The velocity field on the surface of the fluid, $\boldsymbol{u}_s$, can be decomposed into two components: tangential velocity $\boldsymbol{u}_t$ and normal velocity $\boldsymbol{u}_n$,

$$\boldsymbol{u}_s = \boldsymbol{u}(\boldsymbol{X}, t) = \boldsymbol{u}_t(\boldsymbol{X}, t) + \boldsymbol{u}_n(\boldsymbol{X}, t) = \boldsymbol{u}_t(\boldsymbol{X}, t) + u_n(\boldsymbol{X}, t)\boldsymbol{n}, \tag{2.17}$$

where $\boldsymbol{u}_t = \boldsymbol{I}_s \cdot \boldsymbol{u}_s$, $\boldsymbol{u}_n = \boldsymbol{n}\boldsymbol{n} \cdot \boldsymbol{u}_s$ and $\boldsymbol{I}_s = \boldsymbol{I} - \boldsymbol{n}\boldsymbol{n}$ is surface projection operator. Since the interface is axisymmetric, we have $\boldsymbol{u}_t = u_t(\boldsymbol{X}, t)\boldsymbol{t}$, and then the normal and tangential velocity at the interface can be written as follows:

$$u_n = \frac{u - S_z w}{\sqrt{1 + S_z^2}}, \quad u_t = \frac{w + S_z u}{\sqrt{1 + S_z^2}}, \tag{2.18}$$

where $\boldsymbol{u}_s = (u, w)^{\mathrm{T}}$, u and w are the radial and axial components of fluid velocity on the interface, respectively. In light of the aforementioned equations, $\nabla_s \cdot \boldsymbol{u}_s = \nabla_s \cdot \boldsymbol{u}_t + \zeta u_n$ can be applied to (2.16).

Taking the inner product for both sides of (2.16) with $\boldsymbol{n}$ and $\boldsymbol{t}$, respectively, yields the normal and tangential boundary conditions at the interface,

$$\begin{aligned} &-\left\| p_i - \frac{2\mu_i}{1+S_z^2}\left[u_r - S_z(u_z + w_r) + S_z^2 w_z \right] \right\| + \left\| \frac{\varepsilon_i}{2}\frac{1-S_z^2}{1+S_z^2}(\phi_{ir}^2 - \phi_{iz}^2) - 2\varepsilon_i \frac{S_z^2}{1+S_z^2}\phi_{ir}\phi_{iz} \right\| \\ &= \zeta \left[\sigma + (\kappa_s - \mu_s)\left(\frac{(Su_t)_z}{S\sqrt{1+S_z^2}} + \zeta u_n \right) \right] + \frac{2\mu_s}{1+S_z^2}\left[\frac{S_z u_t + u_n}{S^2} - \frac{S_{zz}}{1+S_z^2}\left(\frac{\partial u_t}{\partial z} - \frac{S_{zz} u_n}{1+S_z^2} \right) \right], \end{aligned} \tag{2.19}$$

https://doi.org/10.1017/jfm.2025.10933 Published online by Cambridge University Press

$$-\frac{1}{\sqrt{1+S_z^2}}\left\|2\mu_i\left[u_rS_z+\frac{1}{2}(1-S_z^2)(u_z+w_r)-S_zw_z\right]\right\|+\frac{2\beta}{\sqrt{1+S_z^2}}q(S_z\phi_{i,r}+\phi_{i,z})|_S$$
$$=\frac{\partial\sigma}{\partial z}+\frac{\partial}{\partial z}\left[(\kappa_s-\mu_s)\left(\frac{(Su_t)_z}{S\sqrt{1+S_z^2}}+\zeta u_n\right)\right]+\frac{\sqrt{1+S_z^2}}{S}\frac{\partial}{\partial z}\left[\frac{2\mu_sS}{\sqrt{1+S_z^2}}\left(\frac{\partial u_t}{\partial z}-\frac{S_{zz}u_n}{1+S_z^2}\right)\right]$$
$$-\frac{2\mu_sS_z}{\sqrt{1+S_z^2}}\left[\frac{S_zu_t+u_n}{S^2}-\frac{S_{zz}}{1+S_z^2}\left(\frac{\partial u_t}{\partial z}-\frac{S_{zz}u_n}{1+S_z^2}\right)\right], \tag{2.20}$$

where the subscripts 'r' and 'z' represent the partial derivative.

It should be noted that both the surface shear viscosity $\mu_s(\Gamma)$ and the dilatational viscosity $\kappa_s(\Gamma)$ are functions of the surfactant concentration Γ at the interface. It can be assumed that $\mu_s(\Gamma)$ and $\kappa_s(\Gamma)$ are linearly dependent on Γ (Martínez-Calvo & Sevilla 2018), that is

$$\kappa_s(\Gamma)=\kappa_{sr}\frac{\Gamma}{\Gamma_r},\quad \mu_s(\Gamma)=\mu_{sr}\frac{\Gamma}{\Gamma_r}, \tag{2.21}$$

where the Γ_r represents the reference point for the surfactant concentration, κ_{sr} and μ_{sr} are two constants.

Furthermore, expression of surface tension under an electrical field is elucidated, which is a function of the surfactant concentration and the interfacial electric potential. Prosser & Franses (2001) has provided the formula for calculating the surface tension in the case of over equilibrium, utilizing the chemical potential and the Gibbs adsorption equation. Datwani & Stebe (1999) has also delineated the impact of an excess Maxwell stress on the surface tension generated by the electric potential on the surface. The aforementioned studies have demonstrated that the surface tension can be expressed as the sum of the contributions from the Langmuir isotherms and the electrical effect,

$$\sigma=\sigma_0+R_gT\Gamma_\infty\ln\left(1-\frac{\Gamma}{\Gamma_\infty}\right)+\int_0^{\phi_s}\mathrm{q}\mathrm{d}\phi, \tag{2.22}$$

where σ_0 denotes the surface tension of the cleaning interface, Γ_∞ denotes the maximum packing surfactant concentration and R_g is the gas constant.

2.2. *One-dimensional model*

In light of the elongated thread, the radial reference size R_0 is considerably smaller than the axial reference size L, rendering the one-dimensional model analysis a viable approach. As the outside of the thread is air, whose viscosity is much smaller than the liquid, and air pressure can be assumed to be a constant, under the condition that the maximum electrolyte packing concentration n_s^0 from other electrolytes is far less than the surfactant maximum packing concentration Γ_∞ on the interface, we can derive the one-dimensional long-wave model similar as in Conroy *et al.* (2011). The specific derivation process of the one-dimensional model is outlined in Appendix A.

By choosing the unperturbed radius of the thread R_0 as the length scale, σ_0/μ_1 as the velocity scale, $R_0\mu_1/\sigma_0$ as the time scale, σ_0/R_0 as the pressure scale, k_BT/e as the electric potential scale, $2\Gamma_\infty eN_A$ as scale for the charge density and Γ_∞ as the scale for surfactant concentration, the final dimensionless one-dimensional equations are as follows:

https://doi.org/10.1017/jfm.2025.10933 Published online by Cambridge University Press

$$q_t + q_z w + \frac{1}{2} q w_z = \frac{Pe_s^{-1}}{S} \frac{\partial}{\partial z}(S q_z + S q \phi_{s,z}), \tag{2.23}$$

$$\begin{aligned}
&\left[\frac{S}{2} Re(w_t + w w_z) - 3 S_z w_z - \frac{3}{2} S w_{zz}\right] \\
&\quad + \frac{S}{4} Q \left\{ \chi^2 \phi_s^2 \left[\frac{I_1^2(\chi S)}{I_0^2(\chi S)} - 1 \right] - \frac{\varepsilon_2}{\varepsilon_1} \left[\frac{\phi_s - \phi_w}{S \ln(R_2/S)} \right]^2 \right\}_z + 2\beta q \phi_{s,z} \\
&= \underbrace{\left[\sigma + q(Bo_{\kappa\infty} - Bo_{\mu\infty}) \left(\frac{(Sw)_z}{S} + \zeta(-\frac{S w_z}{2} - S_z w) \right) \right]_z}_{①} \quad \underbrace{}_{②} \\
&\quad - \frac{S}{2} \underbrace{\left\{ \zeta \left[\sigma + q(Bo_{\kappa\infty} - Bo_{\mu\infty}) \left(\frac{(Sw)_z}{S} + \zeta(-\frac{S w_z}{2} - S_z w) \right) \right] \right\}_z}_{③} \quad \underbrace{}_{④} \\
&\quad + \underbrace{\frac{5 Bo_{\mu\infty}}{2S} \cdot \frac{\partial}{\partial z}[q S w_z]}_{⑤},
\end{aligned} \tag{2.24}$$

$$S_t + w S_z + \frac{1}{2} S w_z = 0, \tag{2.25}$$

where

$$\sigma = 1 + \beta \ln(1 - 2q) + \beta q \phi_s - \beta \frac{(\varepsilon_2/\varepsilon_1)\phi_w}{\chi^2 \xi S \ln(R_2/S)} (\phi_s - \Phi), \tag{2.26}$$

$$\phi_s = I_0(\chi S) \frac{\chi^2 \xi q S \ln(R_2/S) + (\varepsilon_2/\varepsilon_1)\phi_w}{\chi I_1(\chi S) S \ln(R_2/S) + (\varepsilon_2/\varepsilon_1) I_0(\chi S)}, \tag{2.27}$$

$$\Phi = \frac{(\varepsilon_2/\varepsilon_1)\phi_w}{\varepsilon_2/\varepsilon_1 + \chi \frac{I_1(\chi S)}{I_0(\chi S)} S \ln(R_2/S)}, \tag{2.28}$$

$$\zeta = \frac{1}{S\sqrt{1 + S_z^2}} - \frac{S_{zz}}{\sqrt{(1 + S_z^2)^3}}. \tag{2.29}$$

The one-dimensional model presented above comprises three independent variables: q represents the surface charge density, which is related to the surfactant concentration, $q = (1/2)\Gamma$ with initial values of q_0 and Γ_0, respectively; w represents the axial velocity, with an initial value of 0; and S indicates the position of the gas–liquid interface.

Equation (2.23) represents the transport equation for the surface charge, with the convection term on the left-hand side and the diffusion term on the right-hand side. Equation (2.24) is a one-dimensional momentum equation. The second and third terms on the left-hand side of the equation represent the electrostatic stress in the bulk stream and the electrostatic tension from the tangential stress equilibrium, respectively. On the right-hand side of this equation, term ① represents the Marangoni stress caused by the spatial inhomogeneity of surface tension and the electrical effect, term ③ is the capillary stress, and terms ②, ④ and ⑤ represent the surface viscous stresses associated with surface dilatational deformation and surface shear deformation.

The dimensionless numbers that appear in the above one-dimensional model are as follows: the Péclet number on the interface $Pe_s = (\sigma_0 R_0)/(D_s \mu)$, the Reynolds

https://doi.org/10.1017/jfm.2025.10933 Published online by Cambridge University Press

number $Re = (\rho\sigma_0 R_0)/(\mu^2)$, the electrostatic Weber number $Q = (\varepsilon_1 k_B T/e)/(\sigma_0 R_0)$ characterizing the ratio of electrostatic stress to capillary stress, the Marangoni number $\beta = R_g T \Gamma_\infty/\sigma_0$ quantifying the sensitivity of surface tension to surfactant concentration, the dilatational Boussinesq number $Bo_{\kappa\infty} = (2\kappa_{sr}\Gamma_\infty)/(\mu_1 R_0 \Gamma_r)$ and the shear Boussinesq number $Bo_{\mu\infty} = (2\mu_{sr}\Gamma_\infty)/(\mu_1 R_0 \Gamma_r)$ used to characterize the relative importance of surface viscosity versus bulk viscosity. Here, an additional parameter $\Theta = \kappa_s/\mu_s = Bo_{\kappa\infty}/Bo_{\mu\infty}$ is introduced to represent the dilatational-to-shear surface viscosity ratio. The remaining parameters in the one-dimensional model are as follows: $\chi = \sqrt{(2R_0^2 e^2 c_0 N_A)/(k_B T \varepsilon_1)}$ represents the ratio of the radius of the liquid thread to the length of Debye, $\xi = \Gamma_\infty/(c_0 R_0)$ is related to the concentration of surfactant and ions in the mainstream, and ϕ_s is the electric potential at the gas–liquid interface.

For an isothermal saturated interface, the Marangoni stress can be neglected, and the only relevant surface stresses are the Young–Laplace pressure and surface viscous stresses (Quéré & de Ryck 1998; Scheid *et al.* 2010; Scheid *et al.* 2012; Martínez-Calvo & Sevilla 2020). Martinez–Calvo provided a detailed description of the applicable conditions, and as discussed by Quéré & de Ryck (1998) in the context of axisymmetric flows, the validity of the assumption is ensured if two conditions are met: first, there must be sufficient surfactant available at the interface during the thinning process; second, the adsorption rate must exceed the characteristic velocity of the interface. This aligns with the diffusion-controlled model and the small Péclet number assumption used in this paper. Furthermore, when the surfactant concentration is low, the influence of the Marangoni effect can similarly be neglected (Ponce-Torres *et al.* 2017), as its impact on the surface tension coefficient is minimal. In addition, the surface viscosity coefficient is difficult to measure under significant Marangoni stress and adsorption dynamics, as all these effects are inherently entangled (Prosser & Franses 2001; Elfring, Leal & Squires 2016). Therefore, although the Marangoni effect was considered during the derivation process, it was neglected in the result calculations, which means $\beta = 0$. This decision is based on two reasons: first, under the aforementioned applicable conditions, neglecting the Marangoni effect is reasonable; second, more importantly, it serves to highlight the influence of surface viscosity, allowing for a more in-depth study of the mechanisms by which surface viscosity and electric effects influence the instability of liquid jets.

If the concentration of the surfactant is set to zero, that is to say the density of the surface charge is also set to zero, then the surface viscosity will also be absent. If the surface viscosity be set to zero, the one-dimensional model will degenerate into the model of Conroy *et al.* (2011).

3. Linear instability analysis

The influence of dimensionless parameters on the dispersion relation is a significant result. Indeed, there are certain dimensionless parameters that have been the subject of prior investigation. Papageorgiu (2002) investigated the impact of surfactants and Reynolds numbers, while Conroy *et al.* (2011) examined the influence of electrostatic and electrokinetic effects, including the electrostatic Weber numbers Q, χ, ξ and so forth, without accounting for surface viscosity. Martínez-Calvo & Sevilla (2018) investigated the impact of surface viscoelasticity induced by surfactants, encompassing dimensionless parameters such as β, $Bo_{\kappa\infty}$, $Bo_{\mu\infty}$ and others. Li & He (2023) conducted a study on the kinetic characteristics of viscoelastic threads containing surfactants and provided a summary of the dimensionless parameters that had been previously selected in studies of surfactant-laden fluids. Among these parameters, the values of Boussinesq numbers were identified as being of particular significance for this paper.

https://doi.org/10.1017/jfm.2025.10933 Published online by Cambridge University Press

Γ_0	$Bo_{\kappa\infty}$	$Bo_{\mu\infty}$	Papers	Type
$0\sim0.5$	0.1	0.1	Ponce-Torres *et al.* (2016*a*)	Theoretical
	$0.14\sim14$	<1.4	Ponce-Torres *et al.* (2020)	Experimental
	675	100	Martínez-Calvo & Sevilla (2018)	Theoretical
	$<<1$	$<<1$	Martínez-Calvo *et al.* (2020)	Theoretical
	0.0143	0.0143	Wee *et al.* (2021)	Theoretical
	$0\sim1000$	$0\sim1$	Herrada *et al.* (2022)	Theoretical

Table 1. The range of surfactant concentrations and the corresponding physical property parameters presented in these literatures when the critical micelle concentration is not reached.

In light of the aforementioned considerations, an investigation is conducted into the combined influence of surface charge density and surface viscosity. Consequently, the initial surface charge density, q_0, and the Boussinesq numbers, $Bo_{\kappa\infty}$ and $Bo_{\mu\infty}$, are the primary variables under consideration. In the absence of special instructions, the following parameters are selected in this section and § 5: interface Péclet number $Pe_s = 10$, Reynolds number $Re = 1$, electrostatic Weber number $Q = 2$, Marangoni number $\beta = 0$ (no Marangoni effect), ratio of liquid thread radius to Debye length $\chi = 1.5$, ratio of surfactant concentration to mainstream ion concentration $\xi = 0.1$, wall potential $\phi_w = 2$, wall radius $R_2 = 5$ and dielectric constant ratio $\varepsilon_2/\varepsilon_1 = 1/80$.

The initial surface charge density and Boussinesq numbers were selected based on the parameter values presented in the surveyed literature, which are listed in table 1. In consideration of the parameter values presented in the aforementioned articles, it can be inferred that the range of surface charge density is 0∼0.25 based on $q_0 = \Gamma_0/2$, while the range of Boussinesq numbers is 0∼100.

The solution to the dispersion relation for the above one-dimensional system (2.23)–(2.25) can be transformed into solving a generalized eigenvalue problem as shown in (3.1),

$$\boldsymbol{A}\begin{bmatrix}\hat{q}\\ \hat{S}\\ \hat{w}\end{bmatrix} = \lambda\boldsymbol{B}\begin{bmatrix}\hat{q}\\ \hat{S}\\ \hat{w}\end{bmatrix}, \tag{3.1}$$

where λ is the growth rate of the perturbation, and $\boldsymbol{A}$ and $\boldsymbol{B}$ are the coefficient matrices. The derivation process is detailed in Appendix B.

Based on the currently selected parameter range, further simplification of (3.1) yields the approximate solution

$$\lambda = \frac{-[6+(9+\Theta)q_0Bo_{\mu\infty}]k^2 + \sqrt{[6+(9+\Theta)q_0Bo_{\mu\infty}]^2k^4 + 8(k^2-k^4)Re}}{4Re}, \tag{3.2}$$

where k is the axial wavenumber. It should be noted that this approximate solution is primarily used to provide a more intuitive understanding of the influence of key parameters on the growth rate. We still prioritize the numerical results obtained from solving (3.1). A comparison between the approximate and numerical solutions is presented in figure 2(*f*), where the discrepancy is insignificant, thereby validating the accuracy of the approximate solution.

Figure 2 illustrates the impact of the initial surface charge density and the two Boussinesq numbers on the dispersion relation, where figure 2(*a–e*) are obtained by numerically solving (3.1). The impact of the initial surface charge density, q_0, on the dispersion curve is illustrated in figure 2(*a*), where the two Boussinesq numbers representing the surface viscosity are set to $Bo_{\kappa\infty} = Bo_{\mu\infty} = 1$. As the initial surface

https://doi.org/10.1017/jfm.2025.10933 Published online by Cambridge University Press

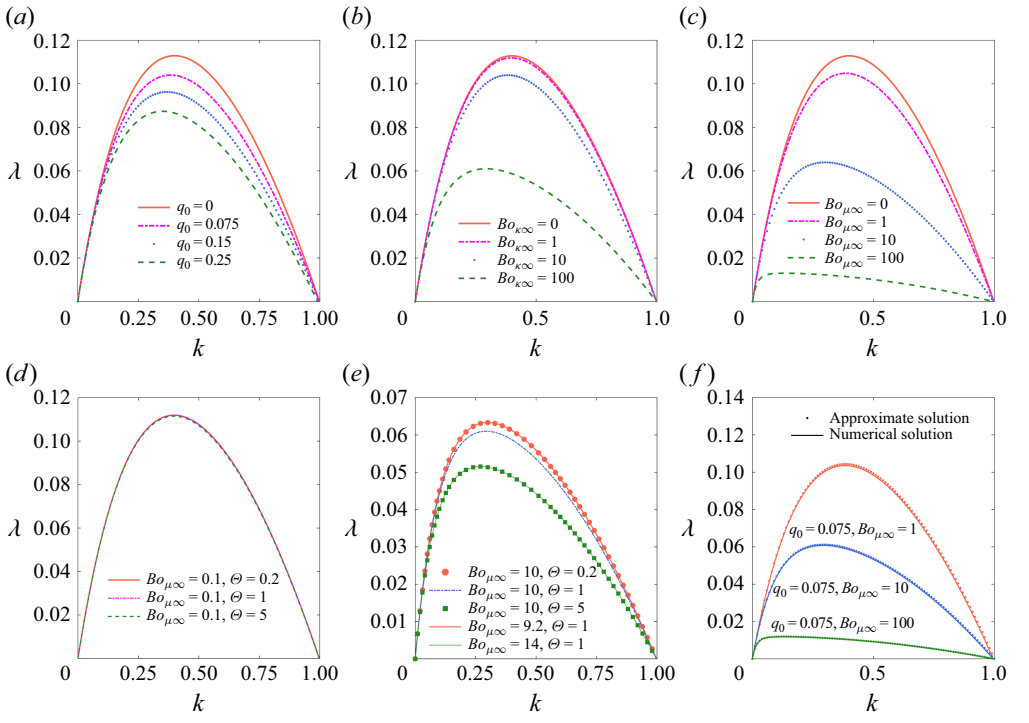


Figure 2. The relation between the growth rate λ and the axial wavenumber k. The effect of (a) the initial surface charge density q_0, with $Bo_{\kappa\infty} = Bo_{\mu\infty} = 1$, ($b$) the dilatational Boussinesq number $Bo_{\kappa\infty}$, with $Bo_{\mu\infty} = 0$, $q_0 = 0.075$, (c) the shear Boussinesq number $Bo_{\mu\infty}$, with $Bo_{\kappa\infty} = 0$, $q_0 = 0.075$ and (d) the dilatational-to-shear surface viscosity ratio Θ for $Bo_{\mu\infty} = 0.1$, $q_0 = 0.075$. (e) Changing Θ or $Bo_{\mu\infty}$ can produce similar effects on the dispersion relation, with $q_0 = 0.075$. (f) Comparison between the approximate solution (3.2) and the numerical solution (3.1).

charge density, q_0, increases, the maximum growth rate, λ_{max}, and the most unstable wavenumber, k_{max}, corresponding to the maximum growth rate, both decrease. In fact, an increase in the initial surface charge density, q_0, results in a greater derivative of the surface potential at the normal transition. This leads to a greater electrostatic stress along the surface, thus enhancing the stability of the thread. This is analogous to the findings of Conroy *et al.* (2011), with the observed trend remaining consistent when surface viscosity is not considered. Figures 2(b) and 2(c) demonstrate the impact of the surface dilatational viscosity Boussinesq number ($Bo_{\kappa\infty}$) and the surface shear viscosity Boussinesq number ($Bo_{\mu\infty}$) on the dispersion relation, respectively, with $q_0 = 0.075$ and another Boussinesq number set to zero. An increase in the two Boussinesq numbers results in a reduction in the maximum growth rate and the most unstable wavenumber, indicating that the surface dilatational viscosity and surface shear viscosity, and the viscous stresses generated by them, exert a stabilizing influence on the liquid thread. The effect of $Bo_{\mu\infty}$ is more pronounced than that of $Bo_{\kappa\infty}$. This is also consistent with the trend obtained by Li & He (2023) without consideration of the electric field.

The influence of the dilatational-to-shear surface viscosity ratio, Θ, on the dispersion relation is examined in figure 2(d) for $q_0 = 0.075$ and $Bo_{\mu\infty} = 0.1$, showing a negligible effect. This can be explained by (3.2), where the perturbation growth rate depends on $[6 + (9 + \Theta)q_0 Bo_{\mu\infty}]$. Since q_0 and $Bo_{\mu\infty}$ are small, even a large Θ contributes minimally. When $Bo_{\mu\infty}$ becomes large, the impact of changing Θ on the dispersion

https://doi.org/10.1017/jfm.2025.10933 Published online by Cambridge University Press

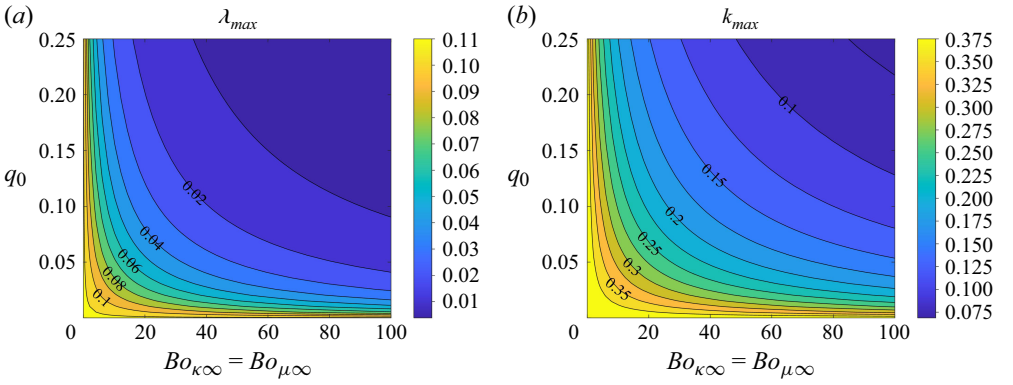


Figure 3. The influence of the initial surface charge density q_0 and the Boussinesq number on (a) the maximum growth rate λ_{max} and (b) the corresponding dominant wavenumber k_{max}.

relation is significant, as can be clearly seen in figure 2(e). However, since the growth rate depends on the product of q_0, $Bo_{\mu\infty}$ and Θ, varying Θ at fixed $Bo_{\mu\infty}$ has a similar effect to varying $Bo_{\mu\infty}$ at fixed Θ, as shown in figure 2(e) (using $Bo_{\mu\infty} = 10$, $\Theta = 1$ as a standard). For instance, the dispersion relations for $Bo_{\mu\infty} = 10$, $\Theta = 5$ and $Bo_{\mu\infty} = 14$, $\Theta = 1$ are nearly identical. This results from the invariance of $[(9 + \Theta)q_0 Bo_{\mu\infty}]$ in both cases.

A similar trend is observed in the nonlinear regime, where Θ must be large to have a noticeable effect. However, surface shear and dilatational viscosities are generally of the same order of magnitude, Θ is unlikely to be very large (Li & He 2023). And the results of changing Θ are analogous to those obtained by varying $Bo_{\mu\infty}$, as briefly analysed at the end of Appendix A. This further indicates that Θ does not alter the fundamental mechanism by which surface viscosity affects thread thinning and suppresses satellite droplet formation. Therefore, in the nonlinear dynamic study of the § 5, we assume $\Theta = 1$, i.e. $Bo_{\kappa\infty} = Bo_{\mu\infty}$, as previously adopted by Ponce-Torres *et al.* (2016*a*), Wee *et al.* (2021) and Li & He (2023).

The phase diagram in figure 3 provides a clear depiction of the monotonic decrease of the maximum growth rate λ_{max} and the most unstable wavenumber k_{max} with increasing initial surface charge density q_0 and Boussinesq numbers, offering key insights for parameter selection and determining the most unstable wavelength in the research of nonlinear dynamics.

4. Numerical method and validation

Equations (2.23)–(2.29) are solved numerically using the finite difference method, specifically employing high-order weighted essentially non-oscillatory schemes. This scheme performs exceptionally well in simulating fine scales and structures (Borges *et al.* 2008). The simulations utilize grids ranging from 800 to 1200 points and time steps from 10^{-5} to 2.5×10^{-5}. The computation is terminated once the radius at the thinnest part of the thread falls below 10^{-4}. The computational domain is determined by the most unstable wavelength for different parameters, i.e. $L_\lambda = 2\pi/k_{max}$.

At the initial time point $t = 0$, the liquid thread is subjected to a small cosine harmonic perturbation,

$$S = 1 - \eta \cos(k_{max} z), \tag{4.1}$$

where k_{max} represents the dimensionless most unstable wavenumber, while η denotes the initial perturbation amplitude. Periodic boundary conditions are applied at $z = -(L_\lambda/2)$

https://doi.org/10.1017/jfm.2025.10933 Published online by Cambridge University Press

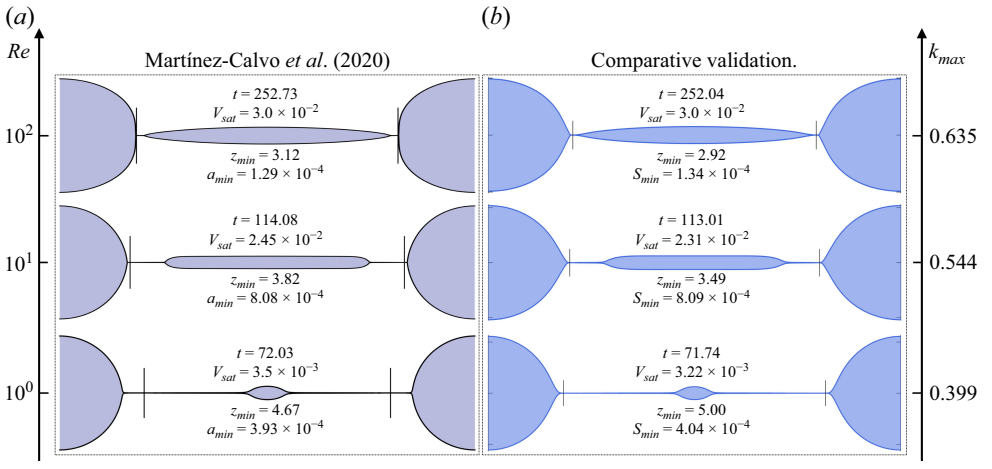


Figure 4. Comparison with the two-dimensional axisymmetric simulation results of Martínez-Calvo *et al.* (2020) (reproduced with permission, Cambridge University Press), focusing on the liquid-thread shape and satellite droplet size at the breakup moment.

and $z = L_\lambda/2$,

$$\begin{aligned} &w(-L_\lambda/2, t) = 0, \quad w(L_\lambda/2, t) = 0, \\ &S_z(-L_\lambda/2, t) = 0, \quad S_z(L_\lambda/2, t) = 0, \\ &q_z(-L_\lambda/2, t) = 0, \quad q_z(L_\lambda/2, t) = 0. \end{aligned} \tag{4.2}$$

To validate the effectiveness of the numerical algorithm and the reliability of the results, firstly, a comparison was made with the two-dimensional axisymmetric simulation results of Martínez-Calvo *et al.* (2020). To align with the model presented in the reference, the model is temporarily simplified as follows: the electric field and surfactant effect are both turned off, i.e. $\phi_w = 0$, $Q = 0$, $Bo_{\kappa\infty} = Bo_{\mu\infty} = 0$, $\beta = 0$, additionally, $Pe_s \to \infty$, and $q_0 = \Gamma_0/2 = 0.5$. The most unstable wavenumber k_{max} is selected based on the dispersion relation from the reference, which is used to determine the most unstable wavelength $L_\lambda = 2\pi/k_{max}$. The initial disturbance amplitude is set to $\eta = 10^{-3}$. The volume fraction of satellite droplet is defined as

$$V_{sat} = \frac{\int_0^{z_{min}} R^2 \mathrm{d}z}{\int_0^{\pi/k_{max}} R^2 \mathrm{d}z}, \tag{4.3}$$

where z_{min} refers to the axial position of the minimum radius of the liquid thread at the end of the calculation. The dimensionless characteristic time is consistent. The comparison between the computational results from the reference and those from the degenerated model in this paper is shown in figure 4. Since the reference did not compute the radius at the thinnest point of the liquid thread to $S_{min} < 1 \times 10^{-4}$, the results corresponding to the time when the liquid thread radius is closest to that in the reference are used for comparison. It can be observed that the interface shape in the computational results matches very well. In terms of quantitative results, there is a slight deviation (approximately 7 %) in the position of the thinnest part of the liquid thread, which is acceptable for a comparison between one-dimensional and two-dimensional models. The deviations in the breakup time and the volume fraction of satellite droplets are also small when compared with the results from the literature. Therefore, it can be concluded that the one-dimensional model and the algorithm used in this study perform well in capturing

https://doi.org/10.1017/jfm.2025.10933 Published online by Cambridge University Press

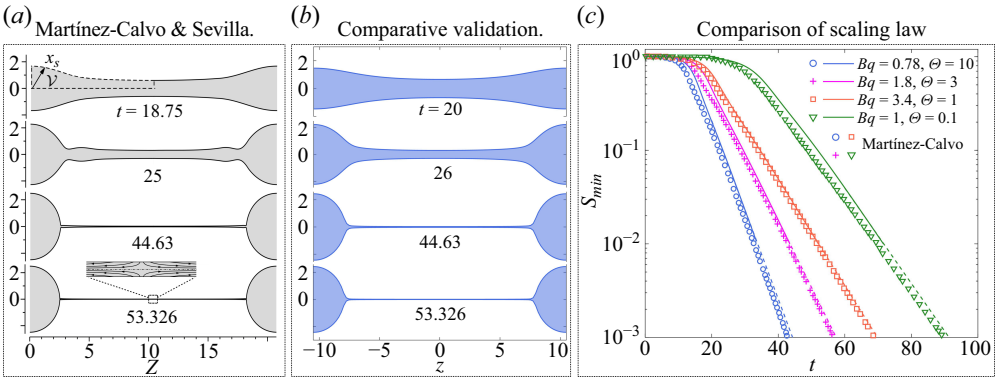


Figure 5. Comparison with the two-dimensional axisymmetric simulation results of Martínez-Calvo & Sevilla (2020) (reproduced with permission, American Physical Society), focusing on the thinning process of the liquid thread and the scaling law.

interface shape development and satellite droplet formation, with negligible differences compared with the two-dimensional axisymmetric simulations.

Additionally, in order to further consider the effect of surface viscosity and make a comparison of the liquid thread thinning process, a comparison with the two-dimensional axisymmetric simulation results from Martínez-Calvo & Sevilla (2020) was also performed. In the literature, the Marangoni effect was neglected, and it was assumed that the surfactant concentration is saturated and the surface viscosity is independent of the surfactant concentration (i.e. μ_s and κ_s are constants). And the time scale is taken as $t_c = (3\kappa_s + \mu_s)/\sigma$, where σ is the surface tension at the saturated surfactant. Some of the parameters are defined as follows: $Bq = \mu_s/(\mu_1 R_0) = Bo_{\mu\infty}/2$, and $\Theta = \kappa_s/\mu_s$. The Reynolds number is set to $Re = 1$, with a constant wavenumber $k = 0.3$, and the dimensionless surfactant concentration is $\Gamma = 1$. The initial disturbance amplitude is set to $\eta = 10^{-3}$.

The images of the liquid thread thinning process and the comparison with the scaling law are shown in figure 5. Figure 5(a) presents the results from the literature for the thinning process of the liquid thread with $Bq = 3.4$ and $\Theta = 1$, while figure 5(b) shows the results of the current one-dimensional model by by disabling the electric field and neglecting the Marangoni effect. A comparison reveals that the overall trend of liquid thread thinning is similar, but the one-dimensional model cannot capture the flow field changes and finer details during this process, such as the significant difference at $t = 25$. However, for the interface shape near rupture, the difference is minimal. In fact, compared with the temporary shape during the thinning process, we are primarily concerned with the shape of the liquid thread close to rupture. Moreover, as seen in figure 5(c), the scaling law of the results from the simplified model closely matches the data extracted from the literature, with only a noticeable delay at $Bq = 1$ and $\Theta = 0.1$. This suggests that the one-dimensional model and the associated algorithm are sufficiently effective in simulating the thinning of the liquid thread.

Based on the comparison with the results from the two aforementioned studies, the validity of the one-dimensional model and the algorithm used in this paper has been verified. This provides strong support and confidence for the validity of the subsequent results.

5. Numerical results for nonlinear dynamics

After validating the model and numerical scheme, the effects of the initial surface charge density, q_0, and the Boussinesq numbers characterizing surface viscosity on the nonlinear

https://doi.org/10.1017/jfm.2025.10933 Published online by Cambridge University Press

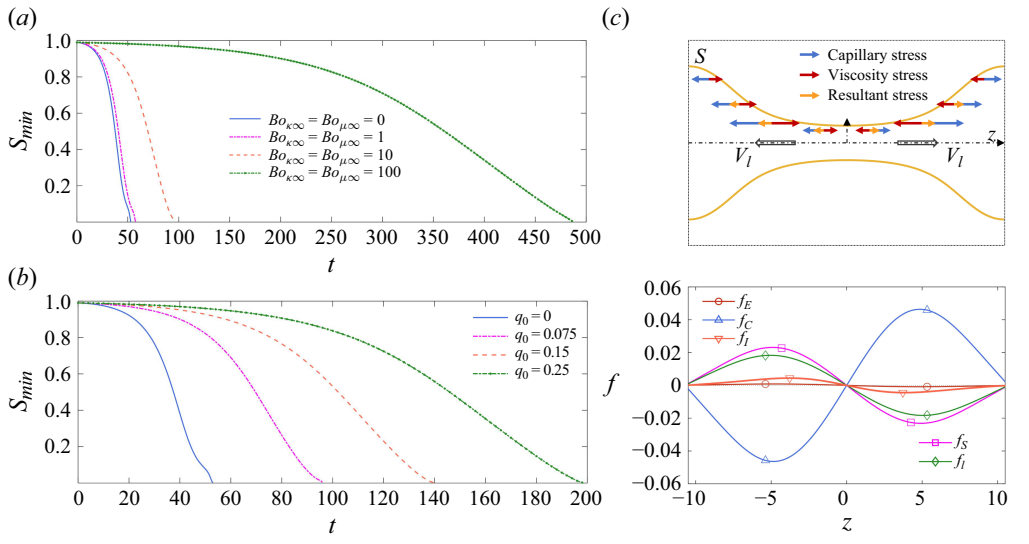


Figure 6. The variation of the radius at the thinnest point of the liquid thread over time. The effects of (*a*) the Boussinesq number and (*b*) the initial surface charge density. (*c*) The contributions of various stresses during the thinning process of the liquid thread with $q_0 = 0.075$, $Bo_{\kappa\infty} = Bo_{\mu\infty} = 10$.

dynamics of the liquid thread are investigated. The study primarily focuses on the thinning dynamics of the liquid thread, the formation of satellite droplets and the underlying mechanisms by which surface viscosity and electrostatic stress influence the process. The dilatational-to-shear surface viscosity ratio is set to $\Theta = 1$, following the analysis in § 3 and the discussion at the end of Appendix A. The initial disturbance amplitude is set to $\eta = 10^{-2}$.

5.1. *The evolution of thread radius over time*

The effects of surface charge density q_0 and the two Boussinesq numbers characterizing surface viscosity on the evolution of the liquid thread over time are illustrated in figure 6. The curves represent the variation of the minimum radius of the liquid thread, S_{min}, over time.

Figure 6(*a*) illustrates the effect of surface viscosity on the thinning dynamics of the liquid thread for $q_0 = 0.075$. Higher Boussinesq numbers significantly delay thinning, with a more pronounced effect at larger values. This result is consistent with the findings of Wee *et al.* (2021) and Li & He (2023). Figure 6(*b*) examines the role of surface charge at $Bo_{\kappa\infty} = Bo_{\mu\infty} = 10$, showing that increased q_0 reduces the thinning rate. This effect primarily arises from enhanced electrostatic repulsion, as the Marangoni effect is neglected here.

For small values of q_0 and the Boussinesq numbers, the S_{min}-time curve exhibits an inflection point when $S_{min} < 0.1$, which disappears at larger values. Initially, the thinnest point of the liquid thread is located at $L_\lambda/2$. As nonlinear effects grow, this thinnest point shifts outward, slowing the thinning rate temporarily before transitioning to an exponential decay. In contrast, at higher q_0 and Boussinesq numbers, the thinning remains centred at $L_\lambda/2$, making this effect less prominent. A detailed explanation follows in § 5.3.

Based on this foundation, the contributions of various stresses during the thinning process of the liquid thread have also been analysed. Considering the conditions $\beta = 0$

https://doi.org/10.1017/jfm.2025.10933 Published online by Cambridge University Press

and $Bo_{\kappa\infty} = Bo_{\mu\infty}$, (2.24) can be rewritten as follows:

$$0 = -Re(w_t + ww_z) + (3w_{zz} + \frac{6}{S}S_z w_z) - \frac{1}{2}Q\left\{\chi^2\phi_s^2\left[\frac{I_1^2(\chi S)}{I_0^2(\chi S)} - 1\right]\right.$$
$$\left. -\frac{\varepsilon_2}{\varepsilon_1}\left[\frac{\phi_s - \phi_w}{S\ln(R_2/S)}\right]^2\right\}_z - [\zeta\sigma]_z + \frac{5Bo_{\mu\infty}}{S^2}\cdot\frac{\partial}{\partial z}[qSw_z]. \tag{5.1}$$

The initial term on the right-hand side of (5.1) represents the inertial stress (f_I), and indeed, the quantity represented by the term ($w_t + ww_z$) characterizes the acceleration. The second term represents the viscous stress exerted by the liquid (f_l), the third term represents the electrostatic stress (f_E), the fourth term represents the capillary stress (f_C) and the fifth term represents the surface shear deformation viscous stress (f_S). By substituting the calculated results into the expressions for each stress, one can determine the instantaneous magnitudes and directions of the stresses, with positive values indicating the positive direction along the z-axis and negative values indicating the opposite.

Figure 6(c) presents the stress balance during the initial and intermediate stages of liquid thread thinning. Capillary stress drives liquid outward, promoting thinning at the centre, while opposing stresses resist this process and inhibit breakup. Computational results confirm that capillary stress oppose other stresses along the z-axis, consistent with the analysis of Wee *et al.* (2021). Under the current parameters, surface shear and bulk viscous stress dominate this resistance, whereas electrostatic effects remain weak due to the low wall potential. A detailed analysis of cases with stronger electrostatic stress follows in subsequent sections.

5.2. *The satellite droplets and main droplets*

The formation of satellite droplets is a topic of great interest among researchers. This study examines the effects of the initial surface charge density q_0 and the Boussinesq numbers characterizing surface viscosity on the formation of satellite droplets.

The sizes of satellite and main droplets are characterized by their equivalent radius, R_s and R_m, respectively. The equivalent radius is defined as $R_{s,m} = (3V_{s,m}/4\pi)^{1/3}$, where V_s and V_m denote the volumes of the satellite and main droplets. These volumes are obtained by integrating the interface shape at the moment of breakup.

Figure 7 illustrates the influence of q_0 and the Boussinesq numbers on satellite droplet formation. Increasing q_0 at fixed Boussinesq numbers (figure 7a,b) or increasing Boussinesq numbers at fixed q_0 (figure 7a,c and 7b,d) leads to smaller satellite droplets, consistent with the experimental findings of Ponce-Torres *et al.* (2017), which demonstrated that surface viscosity reduces satellite droplet size. The details of a qualitative comparison with this experiment are presented in Appendix C. When both parameters are sufficiently large, satellite droplets nearly vanish (figure 7d), suggesting a threshold in the (q_0, $Bo_{\mu\infty}$) space beyond which satellite formation is suppressed.

Figure 7(e) presents the phase diagram delineating the boundary for satellite droplet formation, defined by whether the thread radius at the midpoint exceeds 10^{-3} at the end of the simulation. Red inverted triangles denote cases without satellite droplets, blue circular markers indicate their presence and green squares represent the transitional boundary. This boundary is specific to the current parameter set and may shift with variations in other parameters, such as wall potential. The phase diagram reveals that increasing q_0 and the Boussinesq numbers inhibits satellite droplet formation, primarily due to the reduced maximum growth rate. Although a small most unstable wavenumber typically favours

https://doi.org/10.1017/jfm.2025.10933 Published online by Cambridge University Press

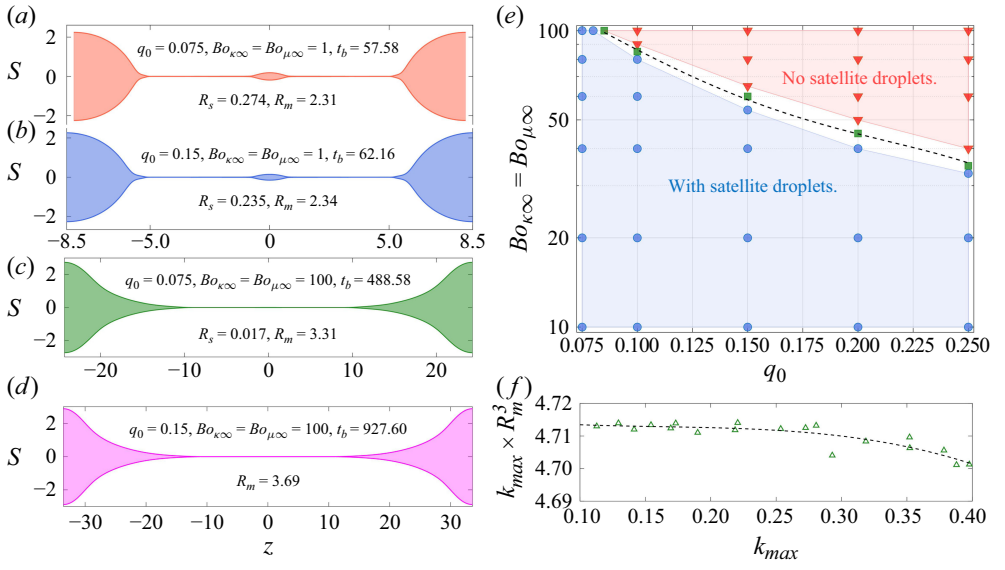


Figure 7. The effect of initial charge density and the Boussinesq numbers on the size of satellite and primary droplets at the breakup moment. (*a–d*) An increase in initial charge density and the Boussinesq numbers reduces the satellite droplet size while enlarging the primary droplet. (*e*) Phase diagram and boundary separating the presence and absence of satellite droplets. (*f*) The equivalent radius of the primary droplet, R_m, exhibits a reliable correlation with the most unstable wavenumber, k_{max}.

satellite formation, the dominant effects of surface charge and viscosity counteract this trend.

In addition to satellite droplets, the size of the primary droplets is also a significant result in liquid stability studies since Lord Rayleigh's seminal work (Rayleigh 1878).

Figure 7(*a–d*) illustrates that as q_0 or the Boussinesq numbers increase, the main droplet radius R_m also increases. This is attributed to the decrease in the most unstable wavenumber, which leads to a longer dominant wavelength and, consequently, a larger primary droplet. However, the main droplet radius maintains a robust correlation with the wavenumber. As shown in figure 7(*f*), $k_{max} \times R_m^3$ approaches a constant value of approximately $1.5\pi \approx 4.712$, with the black dashed line representing the fitted curve. As k_{max} increases, $k_{max} \times R_m^3$ gradually declines, as lower surface charge and Boussinesq numbers promote satellite formation.

5.3. *The mechanism by which surface viscosity suppresses satellite droplet formation*

Section 5.2 shows that higher surface viscosity suppresses satellite droplet formation, warranting further investigation of the underlying mechanisms. We compare two cases: $Bo_{\kappa\infty} = Bo_{\mu\infty} = 1$ (figure 8*a–e*) and $Bo_{\kappa\infty} = Bo_{\mu\infty} = 100$ (figure 8*g–n*), both with $q_0 = 0.075$. Since electrostatic stress is negligible here (§ 5.1), the dominant stresses are capillary stress f_C and viscous stress f_V, with $f_V = f_S + f_l$, where f_S and f_l denote surface shear and bulk viscosity stress, respectively.

For $Bo_{\kappa\infty} = Bo_{\mu\infty} = 1$, the breakup occurs at $t_b = 57.6$. Figure 8(*a*) depicts the evolution of the liquid thread for $t \in [0, 54]$. At $t = 54$, the central section within a single wavelength forms an elongated liquid bridge. If this evolution continues, a satellite droplet will emerge at the midpoint, with the neck point forming between the main and satellite droplets. During thinning, capillary stress drives liquid outward, while viscosity resists this motion. As the bridge region ($z \in [-5, 5]$) becomes thinner, viscous effects

https://doi.org/10.1017/jfm.2025.10933 Published online by Cambridge University Press

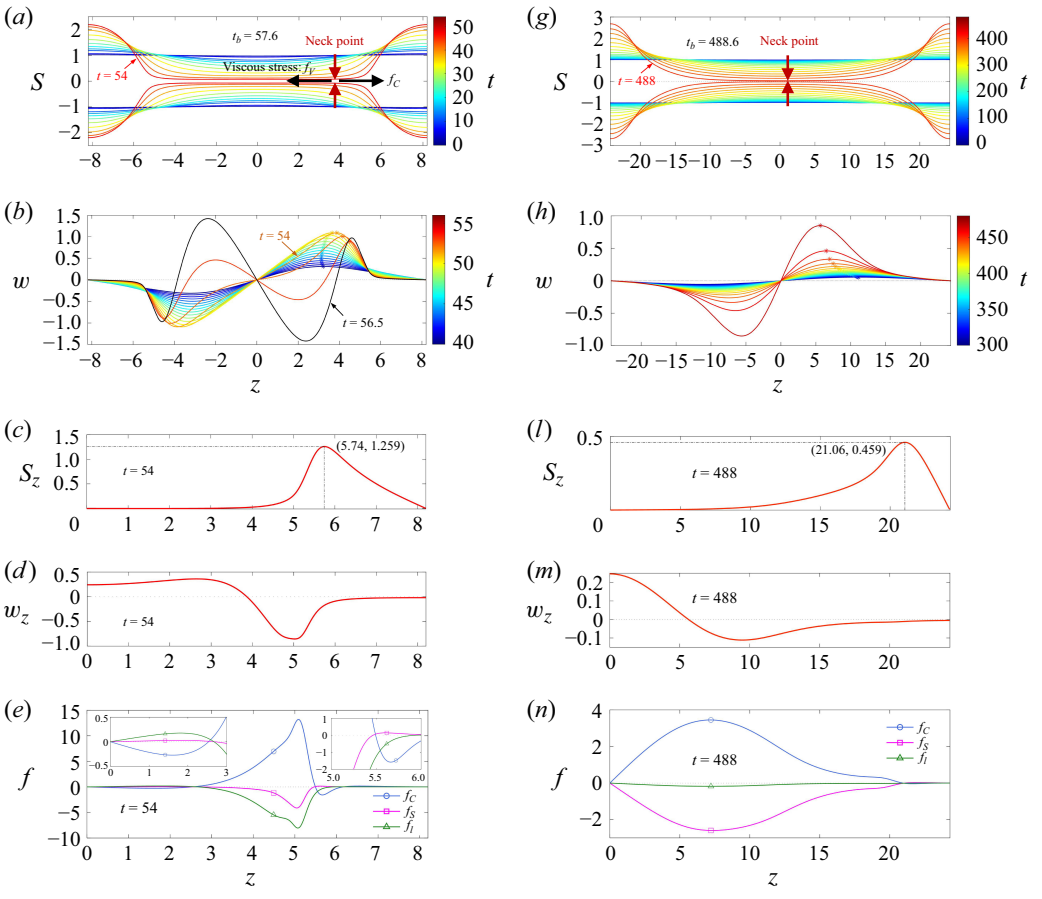


Figure 8. Under a small Boussinesq number $Bo_{\kappa\infty} = Bo_{\kappa\infty} = 1$, panel (*a*) shows the thinning process of the liquid thread, panel (*b*) illustrates the variation of velocity distribution over time, panel (*c*) presents the distribution of the liquid thread radius gradient S_z at $t = 54$, panel (*d*) depicts the velocity gradient w_z at $t = 54$ and panel (*e*) displays the distribution of various stresses at $t = 54$. For a large Boussinesq number $Bo_{\kappa\infty} = Bo_{\kappa\infty} = 100$, panel (*g*) depicts the thinning process of the liquid thread, panel (*h*) shows the velocity distribution over time, panel (*l*) presents the liquid thread radius gradient S_z at $t = 488$, panel (*m*) illustrates the velocity gradient w_z at $t = 488$ and panel (*n*) displays the distribution of various stresses at $t = 488$. The initial charge density is $q_0 = 0.075$ for all cases.

intensify, preventing complete liquid expulsion. Only the outer regions ($z \notin [-4, 4]$) experience significant drainage, leading to liquid retention at the centre and an outward shift of the neck point. Figure 8(*b*) shows that the maximum velocity location (asterisk) moves outward as the thread thins, indicating that the site of maximum instantaneous liquid expulsion shifts outward, which drives the neck point's migration. Near breakup ($t = 56.5$), velocity in the central region reverses, suggesting liquid accumulation at the midpoint to form a satellite droplet. From (5.1), the radius gradient S_z and velocity gradient w_z play a crucial role in balancing capillary and viscous stresses. Figure 8(*c–e*) show that stress peaks closely align with the peak of w_z, with a trend of stress reversal near the bridge centre.

For $Bo_{\kappa\infty} = Bo_{\mu\infty} = 100$, the breakup occurs at $t_b = 488.6$. Figure 8(*g*) shows the evolution of the liquid thread for $t \in [0, 488]$, where the neck point remains at the centre throughout thinning, and no elongated liquid bridge forms. Without such a bridge,

https://doi.org/10.1017/jfm.2025.10933 Published online by Cambridge University Press

capillary stress continuously drives liquid outward, maintaining the neck point at the centre. From the velocity distribution in figure 8(*h*), the maximum velocity point shifts inward, accelerating liquid outflow near the centre and ensuring that the thinnest region remains at the midpoint. This behaviour contrasts sharply with the $Bo_{\mu\infty} = 1$ case, where the film shape near breakup exhibits steeper gradients, leading to bridge formation. The presence of a liquid bridge is a key determinant of satellite droplet formation. A higher surface viscosity suppresses surface gradients, as surfactant accumulation in thicker regions enhances local viscosity, leading to a smoother film profile that prevents bridge formation and inhibits satellite droplet generation. Figure 8(*l*) further confirms that the thickness gradient S_z is significantly lower for $Bo_{\mu\infty} = 100$ than for $Bo_{\mu\infty} = 1$. The velocity gradient influences stress, which in turn affects the velocity distribution, driving the inward movement of the velocity peak.

It is worth noting that the above analysis is based on the influence of interfacial viscosity on the drainage rate and the morphology of the liquid thread, and it has already been stated at the beginning of this section that the effect of the electric field under the present conditions is weak. In § 5.4, we will further demonstrate that the decisive factor governing the distribution of surfactant concentration is the thread radius, while the electric field plays only a secondary role. This implies that the electric field cannot significantly modify the role of interfacial viscosity by altering the surfactant distribution. Therefore, the suppression of drainage and the inhibition of satellite droplet formation by interfacial viscosity can be regarded as intrinsic features, independent of the applied electric field. Consequently, it may be anticipated that the same interfacial-viscosity-driven mechanism would persist even in the presence of an axial electric field, which is not considered in the present work.

5.4. *The mechanism of electrostatic stress and synergy with viscous stress*

In the results presented in § 5.1, the electric stress was relatively small and did not significantly influence the breakup of the liquid thread. All aforementioned results were obtained with a wall potential of $\phi_w = 2$. Therefore, to investigate how the results differ when the electric stress is comparable in magnitude to the viscous stress induced by surface shear deformation, it is worthwhile studying the effects of increasing the wall potential to enhance the electric stress.

In fact, Conroy *et al.* (2011) indicated that as the wall potential increases, the electric stress rises, thereby enhancing the stability of the liquid thread. However, Conroy's model did not account for the issue of surface viscosity. Here, by considering the surface viscosity introduced by surfactants, some different results have been observed.

The influencing factors of electric stress are first explored. The parameters are set as $q_0 = 0.1$ and $Bo_{\kappa\infty} = Bo_{\mu\infty} = 10$. Figure 9(*a*) presents the effect of wall potential on the dispersion relation from linear stability results, showing that an increase in wall potential slightly reduces the maximum growth rate, though the variation is minimal, indicating a negligible influence. However, figure 9(*b*) reveals that a higher wall potential prolongs the final stage of liquid thread thinning, highlighting the significant role of electric stress in this phase. The study by Lakdawala *et al.* (2016) has also demonstrated that the influence of electric effects becomes significantly more pronounced in the final stage of liquid thread thinning compared with its early evolution.

From (5.1), the electric stress f_E depends on the product of the surface potential ϕ_s and its gradient $\phi_{s,z}$. According to (2.27), ϕ_s is negatively correlated with surface charge density q. In addition, from figure 9(*d*) and the charge distribution q in figure 9(*e*), it is clear that the dominant factor controlling the charge concentration is the thread radius S.

https://doi.org/10.1017/jfm.2025.10933 Published online by Cambridge University Press

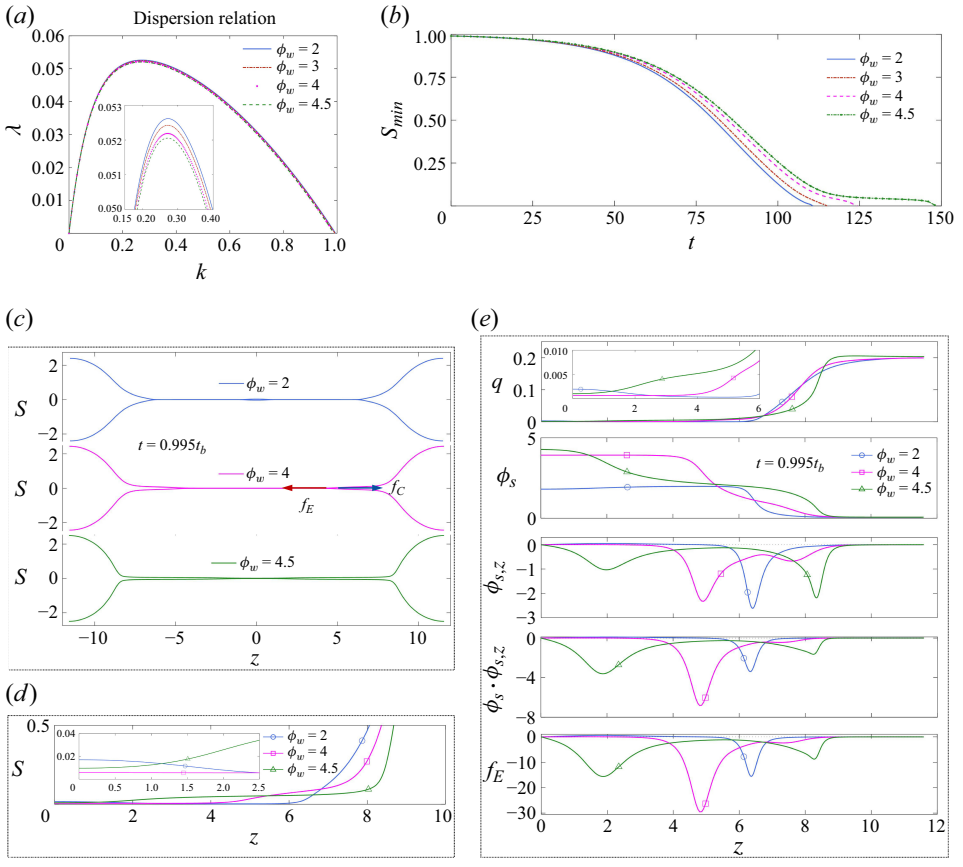


Figure 9. The influencing factors of electrostatic stress. (*a*) The effect of wall potential ϕ_w on the dispersion relation. (*b*) The influence of wall potential ϕ_w on the thinning process of the liquid thread. (*c*) The shape of the liquid thread near rupture under different wall potentials. (*d*) An enlarged view of the liquid thread shape approaching rupture. (*e*) The distributions of charge density, surface potential, surface potential gradient, the product $\phi_s \cdot \phi_{s,z}$ and the electrostatic stress. The parameter values are set as $q_0 = 0.1$ and $Bo_{\kappa\infty} = Bo_{\kappa\infty} = 10$. We select the moment at $t = 0.995t_b$, where t_b is the breakup time.

Thus, the liquid thread radius influences the magnitude of electric stress, which in turn tends to draw liquid from the main droplet towards the origin. This effect becomes more pronounced as the wall potential increases. The results in figure 9(*c–e*) support these analyses. Figure 9(*c–d*) depict the liquid thread radius near rupture under different wall potentials, while figure 9(*e*) shows surface charge density, revealing a strong positive correlation with thread radius. The surface potential ϕ_s is negatively correlated with q, while electric stress f_E follows the trend of $\phi_s \cdot \phi_{s,z}$.

To further analyse the electric potential and field distribution for $\phi_w = 4.5$, the results are computed using (A35)–(A37) and presented in figure 10(*a*). The red curve marks the liquid thread interface. Although $R_2 = 5$, only the region $r < 3$ is shown. The electric field outside the liquid thread is nearly perpendicular to the interface. Since the surfactant adsorbed on the surface carries a positive charge, it experiences an electric pressure that forces liquid outward at satellite droplets, leading to their reduction. This observation aligns with the findings of Conroy *et al.* (2011). Inside the liquid thread, according to (A32) and the Debye–Hückel limit, the bulk charge is negative and related to ϕ_{10}. As depicted in

https://doi.org/10.1017/jfm.2025.10933 Published online by Cambridge University Press

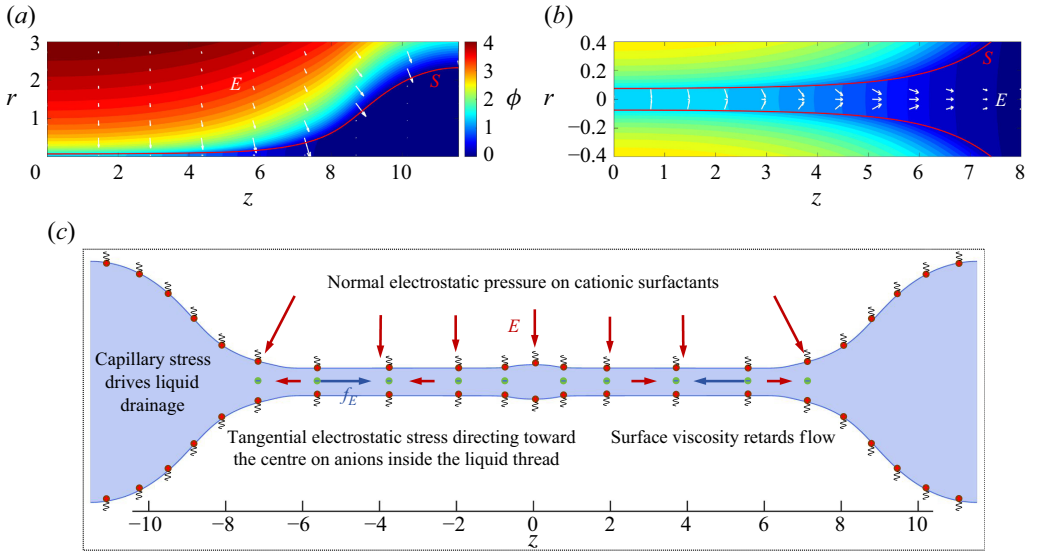


Figure 10. The mechanism of electric effects. (*a*) Distribution of electric potential and field at $\phi_w = 4.5$. (*b*) Local magnification of electric potential and field distribution, focusing on the internal electric field of the liquid thread. (*c*) Schematic model illustrating the twofold effects of electric stresses. Red arrows denote the electric field direction, blue arrows indicate internal electric stress.

figure 10(*b*), the internal electric field has a tangential component directed from the centre towards the ends, generating an electric stress f_E that drives fluid from both ends towards the centre, thereby suppressing liquid drainage. The key influencing factors of f_E have been detailed in figure 9.

Thus, the electric field exerts two primary effects: (i) externally, it applies a normal pressure on the surface-charged surfactant, reducing satellite droplet formation, and (ii) internally, it generates a converging electric stress on the negatively charged bulk, suppressing liquid drainage. The schematic in figure 10(*c*) illustrates these mechanisms. In addition to these electrical effects, capillary stress drives liquid drainage and satellite droplet formation, while surface viscosity counteracts the flow, inhibiting both drainage and satellite droplet formation. Additionally, it should be emphasized that the electric effect influences both the variation in thread thickness and the distribution of surfactants, while the surface charge density q is primarily related to the thread radius S, and surface viscosity is governed by surfactant concentration. Consequently, for the liquid region driven inward by the electric effect ($z \in [-8, -2] \cup [2, 8]$), surface viscosity acts as a stabilizing factor.

Furthermore, ionic surfactants play a key role here by determining the type of surface charge. In conventional electrolyte solutions, the surface charge is governed by the wall potential: a positive wall potential leads to the accumulation of negative charges at the interface. In contrast, for the ionic surfactants considered here, whose adsorption characteristic time is much shorter than the diffusion characteristic time, the surface charge is determined by the type of ions associated with the surfactant (the study of Fauvel *et al.* (2022) can also indirectly support this point). This represents a fundamental difference between ionic surfactants and ordinary electrolytes. A cationic surfactant is chosen specifically in this study to highlight this distinction. At the same time, for an anionic surfactant, similar results to those reported in this work can be obtained if the wall potential is correspondingly adjusted to a negative value.

https://doi.org/10.1017/jfm.2025.10933 Published online by Cambridge University Press

6. Conclusion

This study investigates the nonlinear dynamics of a surfactant-laden thin liquid thread in a radial electric field. A one-dimensional model, with small Reynolds and Péclet numbers, is formulated under the long-wave approximation, followed by linear stability analysis and numerical simulations to explore the nonlinear dynamics, with a particular focus on electric effects and surface viscosity. The key parameters considered include the dimensionless surface charge density, which is directly linked to surfactant concentration, as well as the dilatational and shear Boussinesq numbers. To examine cases where electrostatic and surface viscous stresses are comparable, the wall potential is varied to adjust the electrostatic stress. The study systematically analyses the influence of these parameters on the dynamics of a surfactant-laden liquid thread subjected to small harmonic perturbations in a radial electric field.

The results indicate that both the electrostatic effects of the radial electric field and the surface viscosity of the surfactant inhibit instability by reducing the maximum growth rate, consistent with the findings of Conroy *et al.* (2011) and Martínez-Calvo & Sevilla (2018), respectively. Then, this study further derives an approximate solution to the dispersion relation, theoretically demonstrating that the growth rate is influenced by the product of the initial charge density and the Boussinesq number. In the nonlinear evolution, both electrostatic effects and surface viscosity delay the thinning of the liquid thread and suppress the formation of satellite droplets, aligning with the results of Conroy *et al.* (2011) and Li & He (2023), as well as experimental observations from Ponce-Torres *et al.* (2017). Furthermore, this study explores the mechanism by which surface viscosity inhibits satellite droplet formation and its interaction with electrostatic effects. Surface viscosity suppresses liquid drainage, and this effect is stronger in thicker regions of the thread due to the higher surfactant concentration, which helps maintain the thinnest point at the centre, thereby preventing satellite droplet formation. This is the intrinsic property of interfacial viscosity and is not influenced by the electric field. When the wall potential is large, electrostatic effects become critical near the moment of thread rupture. Externally, electrostatic stress primarily acts as a normal pressure, suppressing satellite droplet formation. Internally, it has a significant tangential component, hindering liquid drainage and delaying rupture. These findings provide practical insights for small-scale liquid threads in applications involving both electric fields and surfactants, such as electrospray inkjet printing and electrospray thrusters (Cheng *et al.* 2022, 2024).

While the one-dimensional model and numerical algorithm presented in this study perform well and offer computational efficiency, a comparison with the results of Martínez-Calvo & Sevilla (2020) clearly highlights the limitations of the one-dimensional model in capturing detailed flow structures. Therefore, high-fidelity, higher-dimensional direct numerical simulations represent a promising avenue for further investigation, enabling more detailed analyses and providing validation for the conclusions drawn in this study, especially the exploration of mechanisms. Furthermore, comparing numerical results with experimental studies remains a valuable direction for future research. Experimental methodologies outlined in López-Herrera & Gañán-Calvo (2004), Ponce-Torres *et al.* (2016*b*) and Ponce-Torres *et al.* (2017) could provide essential guidance for such validation efforts. Moreover, while incorporating the Marangoni effect, electrostatic interactions, surface viscosity and surfactant solubility would significantly increase the complexity of the liquid thread dynamics model, these aspects warrant further investigation. Additionally, the substantial disparity between dilatational and shear surface viscosities – differing by at least an order of magnitude – may lead to intriguing new findings.

https://doi.org/10.1017/jfm.2025.10933 Published online by Cambridge University Press

Moreover, in practical applications such as electrosprays, axial electric fields are often unavoidable. However, Nie *et al.* (2021) demonstrated that radial fields are key to understanding liquid-thread breakup and satellite droplet formation, and noted that the needle–cylinder configuration generating a radial field closely resembles that in realistic electrosprays. Building on this, the present study develops a theoretical model under a purely radial field. The formulation in § 2.1, however, is general and can be adapted to axial fields by modifying the field direction and boundary conditions. In practice, both axial and radial fields need to be considered (Chen *et al.* 2022), but treating them simultaneously remains challenging (Lakdawala *et al.* 2016). Future work may therefore extend the present analysis to axial fields and combine the two effects for closer comparison with experiments.

Acknowledgements. We thank all the reviewers for their constructive comments and suggestions.

Funding. This research was supported by the National Natural Science Foundation of China (grant nos. 12272026, U2341281, 12172317, 12502287) and the Natural Science Foundation of Beijing Municipality (grant no. L248008).

Declaration of interests. The authors report no conflict of interest.

Appendix A.

To begin, we will non-dimensionalize the system of governing equations. Use the scales

$$\begin{gathered}(r, S) = R_0(\hat{r}, \hat{S}), \quad z = L\hat{z}, \quad u_i = \frac{\sigma_0}{\mu_1}\hat{u}_i, \quad w_i = \frac{L\sigma_0}{R_0\mu_1}\hat{w}_i, \quad t = \frac{R_0\mu_1}{\sigma_0}\hat{t}, \\ R_2 = \frac{R_0}{\hat{R}_2}, \quad p = \frac{\sigma_0}{R_0}\hat{p}, \quad \phi_i = \frac{k_BT}{e}\hat{\phi}_i, \quad \boldsymbol{E}_i = \frac{k_BT}{eR_0}\hat{\boldsymbol{E}}_i, \quad c^{\pm} = c_0\hat{c}^{\pm}, \quad \sigma = \sigma_0\hat{\sigma}, \\ \Gamma = \Gamma_\infty\hat{\Gamma}, \quad n^{\pm} = c_0\hat{n}^{\pm}, \quad n_s^{\pm} = n_s^0\hat{n}_s^{\pm}, \quad \rho_i^e = 2c_0eN_A\hat{\rho}_i^e, \quad q = 2\Gamma_\infty eN_A\hat{q},\end{gathered} \tag{A1}$$

where R_0 represents the initial radius of the jet, L is the axial length scale, $\delta = R_0/L$ is a small parameter, k_BT/e is approximately 25 mV for an order 1 electric potential and n_s^0 is the maximum electrolyte packing concentration for other electrolytes unaffected by the surfactant.

In the following content, for simplicity, the hats on the dimensionless quantities will be removed.

First, the Maxwell equation becomes

$$\frac{1}{r}\frac{\partial}{\partial r}\left(r\frac{\partial\phi_i}{\partial r}\right) + \delta^2\frac{\partial^2\phi_i}{\partial z^2} = -\frac{\varepsilon_1}{\varepsilon_i}\chi^2\rho_i^e, \tag{A2}$$

where

$$\chi^2 = \frac{2R_0^2e^2c_0N_A}{k_BT\varepsilon_1}, \tag{A3}$$

$$\rho_1^e = \frac{1}{2}\left(n^{(+)} + c^{(+)} - n^{(-)} - c^{(-)}\right), \quad \rho_2^e = 0. \tag{A4}$$

The dimensionless parameter χ represents the ratio of the jet radius to the Debye length. Region 2 is air, where there are no ions, resulting in a bulk charge density of zero. For the surface charge given by $q = (1/2)\Gamma + (n_s^0/2\Gamma_\infty)(n_s^{(+)} - n_s^{(-)})$, we consider $n_s^0/\Gamma_\infty \ll 1$ to avoid an excess of ion species at the surface and focus on the surfactant, simplifying this to $q = (1/2)\Gamma$.

https://doi.org/10.1017/jfm.2025.10933 Published online by Cambridge University Press

At the interface, the jump conditions are

$$\left(\phi_{1r} - \delta^2 S_z \phi_{1z}\right) - \frac{\varepsilon_2}{\varepsilon_1}\left(\phi_{2r} - \delta^2 S_z \phi_{2z}\right) = \chi^2 \xi q \sqrt{1+\delta^2 S_z^2}, \tag{A5}$$

$$S_z \phi_{1r} + \phi_{1z} = S_z \phi_{2r} + \phi_{2z}. \tag{A6}$$

Here, $\xi = \Gamma_\infty / c_0 R_0$ is related to the ratio of the surfactant concentration to the ion concentration in the main flow. The subscripts 'r' and 'z' denote partial derivatives with respect to r and z, respectively.

The evolution of the positive and negative ion concentrations in the main flow are governed by the Nernst–Planck equation, which can be expressed as

$$\begin{aligned} &\bar{Pe}\left[(n+c)_t^{\pm} + u(n+c)_r^{\pm} + w(n+c)_z^{\pm}\right] \\ &\quad = \frac{1}{r}\frac{\partial}{\partial r}\left[\pm r(n+c)^{\pm}\phi_{1,r} + r(n+c)_r^{\pm}\right] + \delta^2 \frac{\partial}{\partial z}\left[\pm(n+c)^{\pm}\phi_{1,z} + (n+c)_z^{\pm}\right]. \end{aligned} \tag{A7}$$

The dimensionless number that appears is the Péclet number $\bar{Pe} = \sigma_0 R_0 / \omega k_B T \mu_1$, which represents the ratio of the flow velocity to the charge diffusion velocity.

Following the methodology presented by Kas-Danouche, Papageorgiou & Siegel (2009), we can derive the scalar form of the dimensionless surfactant concentration evolution equation,

$$\begin{aligned} &\Gamma_t + \frac{\delta^2 S_t S_z \Gamma_z}{1+\delta^2 S_z^2} + \frac{1}{S\sqrt{1+\delta^2 S_z^2}}\frac{\partial}{\partial z}\left[\frac{S\Gamma(w+\delta^2 u S_z)}{\sqrt{1+\delta^2 S_z^2}}\right] + \frac{\Gamma(u - wS_z)}{S(1+\delta^2 S_z^2)}\left(1 - \frac{\delta^2 S S_{zz}}{1+\delta^2 S_z^2}\right) \\ &\quad = \frac{\bar{Pe}_s^{-1}\delta^2}{S\sqrt{1+\delta^2 S_z^2}}\frac{\partial}{\partial z}\left(\frac{S\Gamma_z + S\Gamma\phi_{s,z}}{\sqrt{1+\delta^2 S_z^2}}\right), \end{aligned} \tag{A8}$$

where the Péclet number at the interface is defined as $\bar{Pe}_s = \sigma_0 R_0 / D_s \mu_1$.

The dimensionless forms of the continuity equation and the momentum equation are given by

$$\frac{1}{r}\frac{\partial}{\partial r}(r u_i) + \frac{\partial w_i}{\partial z} = 0, \tag{A9}$$

$$\bar{Re}_i\left(\frac{\partial u_i}{\partial t} + u_i\frac{\partial u_i}{\partial r} + w_i\frac{\partial w_i}{\partial z}\right) = -\frac{\partial p_i}{\partial r} - Q\chi^2\rho_i^e\frac{\partial \phi_i}{\partial r} + m_i\left(\nabla^2 u_i - \frac{u_i}{r^2}\right), \tag{A10}$$

$$\bar{Re}_i\left(\frac{\partial w_i}{\partial t} + u_i\frac{\partial w_i}{\partial r} + w_i\frac{\partial w_i}{\partial z}\right) = -\delta^2\frac{\partial p_i}{\partial z} - \delta^2 Q\chi^2\rho_i^e\frac{\partial \phi_i}{\partial z} + m_i\nabla^2 w_i, \tag{A11}$$

$$\nabla^2 = \frac{\partial^2}{\partial r^2} + \frac{1}{r}\frac{\partial}{\partial} + \delta^2\frac{\partial^2}{\partial z^2}. \tag{A12}$$

Here, the dimensionless numbers that appear are

$$\bar{Re}_i = \frac{\rho_i \sigma_0 R_0}{\mu_1^2}, \quad m_i = \frac{\mu_i}{\mu_1}, \quad Q = \frac{\varepsilon_1 (k_B T/e)^2}{\sigma_0 R_0}, \quad Q_i = Q\frac{\varepsilon_i}{\varepsilon_1}. \tag{A13}$$

These three dimensionless numbers represent the Reynolds number, the viscosity ratio and the electrostatic Weber number, respectively.

https://doi.org/10.1017/jfm.2025.10933 Published online by Cambridge University Press

At the interface, substituting $q = \Gamma/2$ into (2.19)–(2.21), the dimensionless normal and tangential stress balance conditions are

$$
\begin{aligned}
&-\left\| p_i - \frac{2m_i}{1+\delta^2 S_z^2}\left[u_r - S_z\left(\delta^2 u_z + w_r\right) + \delta^2 S_z^2 w_z\right]\right\| \\
&\quad + \left\| \frac{Q_i}{2}\frac{1-\delta^2 S_z^2}{1+\delta^2 S_z^2}\left(\phi_{i,r}^2 - \delta^2\phi_{i,z}^2\right) - 2Q_i\frac{\delta^2 S_z}{1+\delta^2 S_z^2}\phi_{i,r}\phi_{i,z}\right\| \\
&\quad = \zeta\left[\sigma + (qBo_{\kappa\infty} - qBo_{\mu\infty})\left(\frac{(Su_t)_z}{S\sqrt{1+\delta^2 S_z^2}} + \zeta u_n\right)\right] \\
&\quad + \frac{2qBo_{\mu\infty}}{1+\delta^2 S_z^2}\left[\frac{S_z u_t + u_n}{S^2} - \frac{\delta^2 S_{zz}}{1+\delta^2 S_z^2}\left(\frac{\partial u_t}{\partial z} - \frac{\delta^2 S_{zz} u_n}{1+\delta^2 S_z^2}\right)\right], \qquad \text{(A14)} \\
&-\frac{1}{\sqrt{1+\delta^2 S_z^2}}\left\| 2m_i\left[u_r S_z + \frac{1}{2}(1-\delta^2 S_z^2)(u_z + \delta^{-2} w_r) - S_z w_z\right]\right\| \\
&\quad + \frac{1}{\sqrt{1+\delta^2 S_z^2}} 2\beta q (S_z\phi_{i,r} + \phi_{i,z})|_S \\
&\quad = \frac{\partial\sigma}{\partial z} + \frac{\partial}{\partial z}\left[(qBo_{\kappa\infty} - qBo_{\mu\infty})\left(\frac{(Su_t)_z}{S\sqrt{1+\delta^2 S_z^2}} + \zeta u_n\right)\right] \\
&\quad + \frac{\sqrt{1+\delta^2 S_z^2}}{S}\cdot\frac{\partial}{\partial z}\left[\frac{2qBo_{\mu\infty}S}{\sqrt{1+\delta^2 S_z^2}}\left(\frac{\partial u_t}{\partial z} - \frac{\delta^2 S_{zz} u_n}{1+\delta^2 S_z^2}\right)\right] \\
&\quad - \frac{2qBo_{\mu\infty}S_z}{\sqrt{1+\delta^2 S_z^2}}\left[\frac{S_z u_t + u_n}{S^2} - \frac{\delta^2 S_{zz}}{1+\delta^2 S_z^2}\left(\frac{\partial u_t}{\partial z} - \frac{\delta^2 S_{zz} u_n}{1+\delta^2 S_z^2}\right)\right], \qquad \text{(A15)}
\end{aligned}
$$

where

$$
u_t = \frac{w + \delta^2 S_z u}{\sqrt{1+\delta^2 S_z^2}}, \quad u_n = \frac{u - S_z w}{\sqrt{1+\delta^2 S_z^2}}, \quad \zeta = \frac{1}{S\sqrt{1+\delta^2 S_z^2}} - \frac{\delta^2 S_{zz}}{(1+\delta^2 S_z^2)^{3/2}}. \qquad \text{(A16)}
$$

The newly introduced dimensionless numbers are

$$
Bo_{\kappa\infty} = \frac{2\kappa_{sr}\Gamma_\infty}{\mu_1 R_0 \Gamma_r}, \quad Bo_{\mu\infty} = \frac{2\mu_{sr}\Gamma_\infty}{\mu_1 R_0 \Gamma_r}, \quad \beta = \frac{R_g T\Gamma_\infty}{\sigma_0} = \frac{N_a k_B T\Gamma_\infty}{\sigma_0}, \qquad \text{(A17)}
$$

where the coefficient '2' arises from the relation $\Gamma = 2q$.

The dimensionless expression for the surface tension can be obtained as

$$
\sigma = 1 + \beta\ln(1-2q) + 2\beta\int_0^{\phi_s} q\,\mathrm{d}\phi. \qquad \text{(A18)}
$$

Finally, the kinematic condition can be non-dimensionalized as

$$
u_i = S_t + w_i S_z. \qquad \text{(A19)}
$$

The derivation of the long-wave model is similar to Conroy *et al.* (2011). In the following, we give a very brief discussion. We take the small Reynolds number limit to

https://doi.org/10.1017/jfm.2025.10933 Published online by Cambridge University Press

balance the viscous stresses and capillary stress (Conroy *et al.* 2011). Martínez-Calvo & Sevilla (2020) studied the case where only the bulk viscous stress balances the interfacial tension. In the case where the characteristic size of the liquid jet is small (e.g. 100 μm) and viscous stresses play a key role, the characteristic velocity scale is the viscocapillary velocity (Martínez-Calvo & Sevilla 2018), resulting in a small Reynolds number. For example, considering polydimethylsiloxane oil with a viscosity of $\mu = 0.1-10$ Pa s, density $\rho \approx 970\,\mathrm{kg\,m^{-3}}$ and surface tension $\sigma_0 \approx 21.1\,\mathrm{mN\,m^{-1}}$, the Reynolds number ranges from $10^{-4} \lesssim Re \lesssim 1$. In this case of fine liquid jets with high viscosity, considering $10^{-9} \lesssim D_s \lesssim 10^{-8}$, the Péclet number may fall within the range $1 \lesssim Pe_s \lesssim 10^4$, indicating that diffusion cannot be ignored. Therefore, the small Péclet number assumption is also used here to retain the diffusion term in the model. Since the outside of the thread is air, we assume $\mu_2 = O(\delta^2)$. Dropping the subscript 'i' for velocity and pressure but retaining the subscript for the electric potential, the appropriate expansions for the bulk quantities, which depend on (r,z,t), are

$$w = w_0 + \delta^2 w_1 + \cdots, \tag{A20}$$

$$u = u_0 + \delta^2 u_1 + \cdots, \tag{A21}$$

$$p = p_0 + \delta^2 p_1 + \cdots, \tag{A22}$$

$$\phi_i = \phi_{i0} + \delta^2 \phi_{i1} + \cdots, \tag{A23}$$

$$c^{\pm} = c_0^{\pm} + \delta^2 c_1^{\pm} + \cdots, \quad n^{\pm} = n_0^{\pm} + \delta^2 n_1^{\pm} + \cdots. \tag{A24}$$

The surface quantities, which depend on (z, t), are expanded as

$$\sigma = \sigma_0 + \delta^2 \sigma_1 + \cdots, \tag{A25}$$

$$S = S_0 + \delta^2 S_1 + \cdots, \tag{A26}$$

$$\Gamma = \Gamma_0 + \delta^2 \Gamma_1 + \cdots, \tag{A27}$$

$$q = q_0 + \delta^2 q_1 + \cdots. \tag{A28}$$

Substitute these into the original set of equations and discard terms of order δ^2 and higher.

Considering the small Péclet number assumption $\bar{Pe} \sim \delta^2 Pe$, which implies that the diffusion rate of the surfactant is significantly larger than the convective flow rate of the fluid, the surfactant ion concentration in the bulk flow will be very low. Datwani & Stebe (1999) explains three mechanisms for surfactant mass transfer, with the diffusion-controlled adsorption mechanism indicating that the characteristic diffusion time scale is much larger than the characteristic adsorption time scale. This suggests that the adsorption rate of surfactants is far greater than the diffusion rate. Consequently, we can approximate the bulk concentration of surfactant ions as nearly zero.

The leading order of (A7) is expressed as

$$\frac{1}{r}\frac{\partial}{\partial r}\left[\pm r(n+c)_0^{\pm}\frac{\partial \phi_{10}}{\partial r} + r\frac{\partial (n+c)_0^{\pm}}{\partial r}\right] = 0. \tag{A29}$$

It can thus be demonstrated that

$$\pm (n+c)_0^{\pm}\frac{\partial \phi_{10}}{\partial r} + \frac{\partial (n+c)_0^{\pm}}{\partial r} = 0. \tag{A30}$$

Solving for this yields the following result:

$$(n+c)_0^{\pm} = K_{\pm}\exp(\mp\phi_{10}). \tag{A31}$$

https://doi.org/10.1017/jfm.2025.10933 Published online by Cambridge University Press

The constants $K_\pm$ are integration constants that must satisfy the condition of charge neutrality, given by $(n+c)_0^{\pm}(\phi^0)=1$. From this, we obtain $K_\pm=\exp(\pm\phi^0)$. Further solving the equations gives the volumetric charge density as

$$\rho_1^e \sim \frac{1}{2}\left[(n+c)_0^{(+)}-(n+c)_0^{(-)}\right]=\sinh\left(\phi^0-\phi_{10}\right). \tag{A32}$$

Considering the Debye–Hückel limit at low ion concentrations, where $\left|\phi_{10}-\phi^0\right|\ll 1$, and using the assumption $\phi^0=0$, we can approximate the charge density as $\rho_1^e\approx-\phi_{10}$. Substituting the charge density into (A2), we can solve for the electric potential, and from the boundary conditions, determine the surface charge and surface potential. Equation (A2) can then be written as

$$\frac{1}{r}\frac{\partial}{\partial r}\left(r\frac{\partial\phi_{10}}{\partial r}\right)=\chi^2\phi_{10},\quad \frac{1}{r}\frac{\partial}{\partial r}\left(r\frac{\partial\phi_{20}}{\partial r}\right)=0. \tag{A33}$$

The boundary conditions (A5) and (A6) at $r=S_0(z,t)$ can be rewritten as follows:

$$\phi_{10}=\phi_{20},\quad \frac{\partial\phi_{10}}{\partial r}-\frac{\varepsilon_2}{\varepsilon_1}\frac{\partial\phi_{20}}{\partial r}=\chi^2\xi q_0. \tag{A34}$$

For the bulk region, ϕ_{10} can take the form: $\phi_{10}=\gamma(z,t)I_0(\chi r)+C(z,t)K_0(\chi r)$ Since the potential should remain finite as $r\to 0$, we set $C(z,t)=0$, leading to the simplified form,

$$\phi_{10}=\gamma(z,t)I_0(\chi r). \tag{A35}$$

At the same time, the solution for ϕ_{20} can be obtained in the following form:

$$\phi_{20}=\phi_w+[\phi_s(z,t)-\phi_w]\frac{\ln(r/R_2)}{\ln(S_0/R_2)}, \tag{A36}$$

which satisfies the required boundary conditions.

Upon substituting (A35) and (A36) into the second equation of (A34), the following result is obtained:

$$\gamma(z,t)=\frac{\chi^2\xi q_0 S_0\ln(R_2/S_0)+(\varepsilon_2/\varepsilon_1)\phi_w(t)}{\chi I_1(\chi S_0)S_0\ln(R_2/S_0)+(\varepsilon_2/\varepsilon_1)I_0(\chi S_0)}. \tag{A37}$$

The surface potential is given by the following equation: $\phi_s=\gamma(z,t)I_0(\chi S_0)$. Upon substituting the expression for surface tension and performing the requisite simplifications, the result is

$$\sigma=1+\beta\ln(1-2q_0)+\beta q_0\phi_s-\beta\frac{(\varepsilon_2/\varepsilon_1)\phi_w}{\chi^2\xi S_0\ln(R_2/S_0)}(\phi_s-\Phi), \tag{A38}$$

where

$$\Phi=\frac{(\varepsilon_2/\varepsilon_1)\phi_w}{\varepsilon_2/\varepsilon_1+\chi\frac{I_1(\chi S_0)}{I_0(\chi S_0)}S_0\ln(R_2/S_0)}. \tag{A39}$$

Given that surface charge and surface potential are typically positive, electrostatic effects serve to augment surface tension. Conversely, an increase in the concentration of surfactant has the effect of reducing the surface tension.

Considering $\bar{Pe}_s=\delta^2 Pe_s$, the leading-order expression for the surfactant can be written as

$$\Gamma_{0,t}+\Gamma_{0,z}w+\Gamma_0 w_z+\frac{\Gamma_0 u}{S_0}=\frac{Pe_s^{-1}}{S_0}\frac{\partial}{\partial z}(S_0\Gamma_{0,z}+S_0\Gamma_0\phi_{s,z}). \tag{A40}$$

https://doi.org/10.1017/jfm.2025.10933 Published online by Cambridge University Press

The surface charge density is given by $q_0 = (1/2)\Gamma_0$. From this, we can derive the surface charge evolution equation,

$$q_{0,t} + q_{0,z}w + q_0 w_z + \frac{q_0 u}{S_0} = \frac{Pe_s^{-1}}{S_0}\frac{\partial}{\partial z}(S_0 q_{0,z} + S_0 q_0 \phi_{s,z}). \tag{A41}$$

In the bulk flow of liquid thread, by integrating the momentum equations and applying the boundary conditions, we find that $w_0(z, t)$ is independent of r. Additionally, we have $u_0(r, z, t) = -(r w_{0,z}/2)$. Integration of the leading-order radial momentum equation with respect to r yields the following result:

$$p_0 = \frac{1}{2}Q\chi^2\phi_{10}^2 + K(z, t), \tag{A42}$$

where $K(z, t)$ is the integration constant.

The initial term on the right-hand side of the equation is attributed to the electrical effects, whereas the second term represents the integration constant. The leading-order axial momentum equation is expressed as follows:

$$Re(w_{0,t} + w_0 w_{0,z}) = -\frac{\partial p_0}{\partial z} - Q\chi^2\rho_1^e\frac{\partial \phi_{10}}{\partial r} + w_{0,zz} + \frac{1}{r}\frac{\partial}{\partial r}(r w_{1,r}). \tag{A43}$$

Upon substituting (A42) and using $\rho_1^e \sim -\phi_{10}$ for (A43), the result is

$$Re(w_{0,t} + w_0 w_{0,z}) + K_z(z, t) - w_{0,zz} = \frac{1}{r}\frac{\partial}{\partial r}(r w_{1,r}). \tag{A44}$$

After integrating with respect to r, the following can be obtained:

$$w_1 = \frac{r^2}{4}\left[Re(w_{0,t} + w_0 w_{0,z}) + K_z(z, t) - w_{0,zz}\right] + A(z, t). \tag{A45}$$

Consider the air pressure outsider the thread is a constant $p_2 = p_{air}$, the leading order of the normal stress balance is given by

$$\begin{aligned} &p_0 + w_{0,z} + \frac{\varepsilon_2}{2\varepsilon_1}Q(\phi_{20,r})^2|_s - \frac{1}{2}Q(\phi_{10,r})^2|_s \\ &= \zeta\left[\sigma + q_0(Bo_{\kappa\infty} - Bo_{\mu\infty})\left(\frac{(S_0 w_0)_z}{S_0} + \zeta\left(-\frac{S_0 w_{0,z}}{2} - S_{0,z}w_0\right)\right)\right] - q_0 Bo_{\mu\infty}\frac{w_{0,z}}{S_0}. \end{aligned} \tag{A46}$$

The leading order for the tangential stress continuum is given by

$$\begin{aligned} &\left(-3S_{0,z}w_{0,z} - \frac{S_0}{2}w_{0,zz} + w_{1,r}\right) + 2\beta q_0(S_{0,z}\phi_{10,r} + \phi_{10,z})|_s \\ &\quad = \frac{\partial \sigma}{\partial z} + \frac{\partial}{\partial z}\left[q_0(Bo_{\kappa\infty} - Bo_{\mu\infty})\left(\frac{(S_0 w_0)_z}{S_0} + \zeta\left(-\frac{S_0 w_{0,z}}{2} - S_{0,z}w_0\right)\right)\right] \\ &\quad + \frac{1}{S_0}\frac{\partial}{\partial z}(2q_0 Bo_{\mu\infty}S_0 w_{0,z}) + q_0 Bo_{\mu\infty}S_{0,z}\frac{w_{0,z}}{S_0}. \end{aligned} \tag{A47}$$

Substituting (A42) into (A46) yields

$$\begin{aligned} &\frac{1}{2}Q\left[\chi^2\phi_{10}^2 + \frac{\varepsilon_2}{2\varepsilon_1}(\phi_{20,r})^2 - (\phi_{10,r})^2\right]|_s + K(z, t) + w_{0,z} \\ &= \zeta\left[\sigma + q_0(Bo_{\kappa\infty} - Bo_{\mu\infty})\left(\frac{(S_0 w_0)_z}{S_0} + \zeta\left(-\frac{S_0 w_{0,z}}{2} - S_{0,z}w_0\right)\right)\right] - q_0 Bo_{\mu\infty}\frac{w_{0,z}}{S_0}. \end{aligned} \tag{A48}$$

https://doi.org/10.1017/jfm.2025.10933 Published online by Cambridge University Press

From (A48), we can derive the expression for $K(z,t)$. Upon substituting both (A45) and (A48) into (A47) and performing the requisite simplifications, we obtain

$$\begin{aligned}
&\left[\frac{S_0}{2}Re(w_{0,t}+w_0w_{0,z})-3S_{0,z}w_{0,z}-\frac{3}{2}S_0w_{0,zz}\right]\\
&\quad+\frac{S_0}{4}Q\left\{\chi^2\phi_s^2\left[\frac{I_1^2(\chi S_0)}{I_0^2(\chi S_0)}-1\right]-\frac{\varepsilon_2}{\varepsilon_1}\left[\frac{\phi_s-\phi_w}{S_0\ln(R_2/S_0)}\right]^2\right\}_z+2\beta q_0\phi_{s,z}\\
&\quad=\left[\sigma+q_0(Bo_{\kappa\infty}-Bo_{\mu\infty})\left(\frac{(S_0w_0)_z}{S_0}+\zeta(-\frac{S_0w_{0,z}}{2}-S_{0,z}w_0)\right)\right]_z\\
&\quad-\frac{S_0}{2}\left\{\zeta\left[\sigma+q_0(Bo_{\kappa\infty}-Bo_{\mu\infty})\left(\frac{(S_0w_0)_z}{S_0}+\zeta(-\frac{S_0w_{0,z}}{2}-S_{0,z}w_0)\right)\right]\right\}_z\\
&\quad+\frac{5Bo_{\mu\infty}}{2S_0}\cdot\frac{\partial}{\partial z}[q_0S_0w_{0,z}].
\end{aligned}\tag{A49}$$

The kinematic boundary condition is defined as follows:

$$S_{0,t}+w_0S_{0,z}+\frac{1}{2}S_0w_{0,z}=0.\tag{A50}$$

At this juncture, the streamlined one-dimensional model by using the scales in (A1) can be derived by eliminating the $'0'$ from the subscripts of (A41), (A49) and (A50):

$$q_t+q_zw+\frac{1}{2}qw_z=\frac{Pe_s^{-1}}{S}\frac{\partial}{\partial z}(Sq_z+Sq\phi_{s,z}),\tag{A51}$$

$$\begin{aligned}
&\left[\frac{S}{2}Re(w_t+ww_z)-3S_zw_z-\frac{3}{2}Sw_{zz}\right]\\
&\quad+\frac{S}{4}Q\left\{\chi^2\phi_s^2\left[\frac{I_1^2(\chi S)}{I_0^2(\chi S)}-1\right]-\frac{\varepsilon_2}{\varepsilon_1}\left[\frac{\phi_s-\phi_w}{S\ln(R_2/S)}\right]^2\right\}_z+2\beta q\phi_{s,z}\\
&\quad=\left[\sigma+q(Bo_{\kappa\infty}-Bo_{\mu\infty})\left(\frac{(Sw)_z}{S}+\zeta(-\frac{Sw_z}{2}-S_zw)\right)\right]_z\\
&\quad-\frac{S}{2}\left\{\zeta\left[\sigma+q(Bo_{\kappa\infty}-Bo_{\mu\infty})\left(\frac{(Sw)_z}{S}+\zeta(-\frac{Sw_z}{2}-S_zw)\right)\right]\right\}_z\\
&\quad+\frac{5Bo_{\mu\infty}}{2S}\cdot\frac{\partial}{\partial z}[qSw_z],
\end{aligned}\tag{A52}$$

$$S_t+wS_z+\frac{1}{2}Sw_z=0,\tag{A53}$$

where

$$\sigma=1+\beta\ln(1-2q)+\beta q\phi_s-\beta\frac{(\varepsilon_2/\varepsilon_1)\phi_w}{\chi^2\xi S\ln(R_2/S)}(\phi_s-\Phi),\tag{A54}$$

$$\phi_s=I_0(\chi S)\frac{\chi^2\xi qS\ln(R_2/S)+(\varepsilon_2/\varepsilon_1)\phi_w}{\chi I_1(\chi S)S\ln(R_2/S)+(\varepsilon_2/\varepsilon_1)I_0(\chi S)},\tag{A55}$$

$$\Phi=\frac{(\varepsilon_2/\varepsilon_1)\phi_w}{\varepsilon_2/\varepsilon_1+\chi\frac{I_1(\chi S)}{I_0(\chi S)}S\ln(R_2/S)},\tag{A56}$$

$$\zeta=\frac{1}{S\sqrt{1+\delta^2S_z^2}}-\frac{\delta^2S_{zz}}{(1+\delta^2S_z^2)^{3/2}}.\tag{A57}$$

https://doi.org/10.1017/jfm.2025.10933 Published online by Cambridge University Press

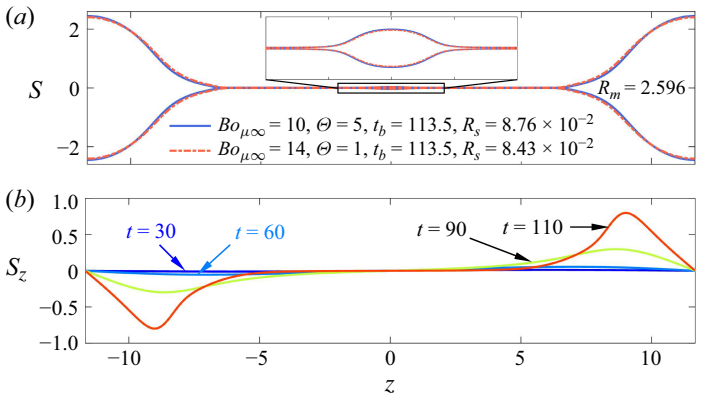


Figure 11. (*a*) Comparison of thread shape and droplet size at the breakup moment for $Bo_{\mu\infty} = 10$, $\Theta = 5$ and $Bo_{\mu\infty} = 14$, $\Theta = 1$, showing nearly identical results. (*b*) Evolution of S_z during thread thinning at different times, with $Bo_{\mu\infty} = 10$, $\Theta = 5$.

After formulating the one-dimensional model, a brief supplementary analysis is conducted to explain why the Boussinesq numbers are set equal in nonlinear dynamic studies (§ 5). Defining the dilatational-to-shear surface viscosity ratio as $\Theta = \kappa_s/\mu_s$, it follows that $\Theta = Bo_{\kappa\infty}/Bo_{\mu\infty}$. For simplification, $\zeta = 1/S$ is introduced, which is a reasonable approximation when S_z is not significantly large. Consequently, the following equation can be obtained:

$$\frac{(Sw)_z}{S} + \zeta\left(-\frac{Sw_z}{2} - S_z w\right) \to \frac{Sw_z}{2S}. \tag{A58}$$

Thus, all terms related to surface viscosity on the right-hand side of (A52) can be simplified as

$$\frac{(9+\Theta)Bo_{\mu\infty}}{4S}[qSw_z]_z. \tag{A59}$$

It can be observed that a significant effect only emerges when Θ is large (need to be at least the order one quantity). However, since surface shear and dilatational viscosities are generally of the same order of magnitude, Θ is unlikely to be very large (Li & He 2023).

On the other hand, (A59) indicates that varying Θ and modifying $Bo_{\mu\infty}$ yield comparable effects. Although the above derivation holds strictly for small S_z, in most cases during the thinning process of the liquid thread, S_z remains relatively small over the entire computational domain, as shown in figure 11(*b*), with $Bo_{\mu\infty} = 10$, $\Theta = 5$. Numerical simulations further confirm that adjusting Θ and $Bo_{\mu\infty}$ produces highly similar results, with the nonlinear simulation incorporating the full expression for curvature, as showed in figure 11(*a*). The numerical computation method is presented in § 4.

This suggests that Θ does not fundamentally alter the role of surface viscosity in the system's dynamics. Furthermore, given that Θ is generally not very large (Li & He 2023), it is reasonable to adopt $\Theta = 1$ for the nonlinear dynamic simulations in § 5, consistent with the approach taken in Ponce-Torres *et al.* (2016*a*), Wee *et al.* (2021) and Li & He (2023).

At the same time, it should be emphasized that the above simplifications (A58) and (A59) are only to justify the choice of $\Theta = 1$. In numerical simulations, the full one-dimensional model is still used.

https://doi.org/10.1017/jfm.2025.10933 Published online by Cambridge University Press

Appendix B.

The process of solving the dispersion relation is as follows.

The linearization of the system of (2.23)–(2.29) is based on the following basic states: $w = 0$, $S = 1$, $q = q_0$, where q_0 is a constant. The fundamental regular mode is expanded as follows:

$$\begin{aligned} w(z,t) &= \hat{w}\mathrm{e}^{\lambda t+ikz} + \text{c.c.} \\ S(z,t) &= 1 + \hat{S}\mathrm{e}^{\lambda t+ikz} + \text{c.c.} \\ q(z,t) &= q_0 + \hat{q}\mathrm{e}^{\lambda t+ikz} + \text{c.c.} \end{aligned} \tag{B1}$$

where the hat represents the perturbation term, k denotes the wavenumber and λ signifies the growth rate of the time instability, 'c.c.' denotes the complex conjugate. Substitution of (B1) into the system of (2.23)–(2.29) allows the linearized system of equations to be obtained by selecting the system of equations composed of the first-order perturbation terms. This process is complex, with the main difficulty lying in the linearization of the ϕ_s and σ functions.

The following represents the linearized system of equations:

$$\frac{1}{2}q_0 ik\hat{w} + Pe_s^{-1}\left[k^2\hat{q} + q_0\left(\phi_{s,q}k^2\hat{q} + \phi_{s,S}k^2\hat{S}\right)\right] = -\lambda\hat{q}, \tag{B2}$$

$$\begin{aligned} &3k^2\hat{w} + 4\beta q_0\left(\phi_{s,q}ik\hat{q} + \phi_{s,S}ik\hat{S}\right) + Q\chi^2\left[I_1^2(\chi) - I_0^2(\chi)\right]\left[\gamma(q_0,1)\right]\left(\gamma_q ik\hat{q} + \gamma_S ik\hat{S}\right) \\ &\quad + \frac{1}{2}Q\chi^3\left[\gamma(q_0,1)\right]^2\left[I_0(\chi) - 2I_1(\chi) + I_2(\chi)\right]ik\hat{(S)} \\ &\quad - Q\frac{\varepsilon_2}{\varepsilon_1}\left[\gamma_{sw}(q_0,1)\right]\left(\gamma_{sw,q}ik\hat{q} - \gamma_{sw,S}ik\hat{S}\right) + \left(\frac{\Theta}{2} + 4.5\right)Bo_{\mu\infty}q_0k^2\hat{w} \\ &\quad - \left[\sigma_q ik\hat{q} + \sigma_S ik\hat{S} - ik\hat{S}\left(k^2-1\right)\sigma(q_0,1)\right] = -Re\lambda\hat{w}, \end{aligned} \tag{B3}$$

$$\frac{1}{2}ik\hat{w} = -\lambda\hat{S}. \tag{B4}$$

The coefficients $\phi_{s,q}(q_0, S_0)$, $\phi_{s,S}(q_0, S_0)$, $\gamma(q_0, S_0)$, $\gamma_q(q_0, S_0)$, $\gamma_S(q_0, S_0)$, $\gamma_{sw}(q_0, S_0)$, $\gamma_{sw,q}(q_0, S_0)$, $\gamma_{sw,S}(q_0, S_0)$, $\sigma(q_0, S_0)$, $\sigma_q(q_0, S_0)$ and $\sigma_S(q_0, S_0)$ are only pertinent to q_0 and S_0, where the value of S_0 is set to $S_0 = 1$. Let $\varepsilon = \varepsilon_2/\varepsilon_1$, these coefficients are expressed as follows:

$$\phi_{s,q} = \frac{\chi^2\xi I_0(\chi)\ln R_2}{\chi I_1(\chi)\ln R_2 + \varepsilon I_0(\chi)}, \tag{B5}$$

$$\phi_{s,S} = \frac{\left\{\begin{array}{l} \varepsilon I_0(\chi)\left[-q_0\chi^2\xi I_0(\chi) + \chi\phi_w I_1(\chi)\right] \\ +\varepsilon\left[\left(-\chi^2\phi_w + q_0\chi^2\xi\right)I_0^2(\chi) + \chi^2\phi_w I_1^2(\chi)\right]\ln R_2 \\ +q_0\chi^3\xi\left[-\chi I_0^2(\chi) + I_0(\chi)I_1(\chi) + \chi I_1^2(\chi)\right] \end{array}\right\}}{\left[\chi I_1(\chi)\ln R_2 + \varepsilon I_0(\chi)\right]^2}, \tag{B6}$$

$$\gamma(q_0,1) = \frac{q_0\chi^2\xi\ln R_2 + \varepsilon\phi_w}{\chi I_1(\chi)\ln R_2 + \varepsilon I_0(\chi)}, \tag{B7}$$

$$\gamma_q = \frac{\chi^2\xi\ln R_2}{\chi I_1(\chi)\ln R_2 + \varepsilon I_0(\chi)}, \tag{B8}$$

https://doi.org/10.1017/jfm.2025.10933 Published online by Cambridge University Press

$$\gamma_S = \frac{\left\{\begin{array}{c} \chi I_1(\chi)\left[\left(\varepsilon-\varepsilon^2\right)\phi_w + q_0\chi^2\xi\left(-\varepsilon+\ln R_2\right)\ln R_2\right] \\ -I_0(\chi)\left[\varepsilon q_0\chi^2\xi + \left(\varepsilon\chi^2\phi_w - \varepsilon q_0\chi^2\xi + q_0\chi^2\xi\ln R_2\right)\ln R_2\right] \end{array}\right\}}{\left[\chi I_1(\chi)\ln R_2 + \varepsilon I_0(\chi)\right]^2}, \tag{B9}$$

$$\gamma_{sw}(q_0, 1) = \frac{q_0\chi^2\xi I_0(\chi) - \chi I_1(\chi)}{\chi I_1(\chi)\ln R_2 + \varepsilon I_0(\chi)}, \tag{B10}$$

$$\gamma_{sw,q} = \frac{\chi^2\xi I_0(\chi)}{\chi I_1(\chi)\ln R_2 + \varepsilon I_0(\chi)}, \tag{B11}$$

$$\gamma_{sw,S} = \frac{\chi\left\{\begin{array}{c} \left(\varepsilon + q_0\chi^2\xi\right)I_0(\chi)I_1(\chi) - \chi I_0^2(\chi)\left(\varepsilon + q_0\chi^2\xi\ln R_2\right) \\ +\chi I_1^2(\chi)\left[-1+\varepsilon+\left(1+q_0\chi^2\xi\right)\ln R_2\right] \end{array}\right\}}{\left[\chi I_1(\chi)\ln R_2 + \varepsilon I_0(\chi)\right]^2}, \tag{B12}$$

$$\sigma(q_0, 1) = 1 + \beta\ln(1-2q_0) + \beta q_0 I_0(\chi)\frac{q_0\chi^2\xi\ln R_2}{\chi I_1(\chi)\ln R_2 + \varepsilon I_0(\chi)}, \tag{B13}$$

$$\sigma_q = \frac{2\beta}{2q_0-1} + \frac{2\beta q_0\chi\xi I_0(\chi)\ln R_2}{\chi I_1(\chi)\ln R_2 + \varepsilon I_0(\chi)}, \tag{B14}$$

$$\sigma_S = \frac{1}{2}\frac{\beta q_0^2\chi^2\xi\left\{\begin{array}{c} -2\varepsilon I_0^2(\chi) + 2\varepsilon I_0^2(\chi)\ln R_2 \\ -\chi^2\left[-2I_1^2(\chi) + I_0^2(\chi) + I_0(\chi)I_2(\chi)\right] \end{array}\right\}}{\left[\chi I_1(\chi)\ln R_2 + \varepsilon I_0(\chi)\right]^2}. \tag{B15}$$

The solution of (B2)–(B4) can be transformed into a generalized eigenvalue problem:

$$\boldsymbol{A}\begin{bmatrix}\hat{q}\\ \hat{S}\\ \hat{w}\end{bmatrix} = \lambda\boldsymbol{B}\begin{bmatrix}\hat{q}\\ \hat{S}\\ \hat{w}\end{bmatrix}, \tag{B16}$$

where $\boldsymbol{A}$ represents the coefficient matrix situated to the left of (B2)–(B4), $\boldsymbol{B} = Diag[-1, -Re, -1]$. The numerical solution of the dispersion relationship can be obtained by solving the generalized eigenvalue problem.

In fact, (B16) can be simplified further. Given the parameters selected at the beginning of this section and the equality of the two Boussinesq numbers, the terms of the smaller magnitude of the coefficient matrix $\boldsymbol{A}$ can be ignored. For instance, for the element in the first row and second column of matrix $\boldsymbol{A}$, $ik(k^2-1) \sim O(10^{-1}\cdot i)$ and $Q\chi^2 ik[I_1^2(\chi) - I_0^2(\chi)][\gamma(q_0, 1)] \sim O(10^{-3}\cdot i)$ can be obtained. Therefore, the latter term is considered negligible due to its small magnitude. After neglecting all the minor terms, the following expression can be obtained:

$$\begin{bmatrix} k^2 + Re\lambda + (\Theta/2 + 4.5)Bo_{\mu\infty}q_0k^2 & ik(k^2-1) & 0 \\ ik/2 & \lambda & 0 \\ ikq_0/2 & 0 & \lambda + Pe_s^{-1}(k^2 + k^2\phi_{s,q}q_0) \end{bmatrix}\begin{bmatrix}\hat{q}\\ \hat{S}\\ \hat{w}\end{bmatrix} = 0. \tag{B17}$$

The approximate solution of the dispersion relation can be derived from the coefficient matrix determinant of (B17) being equal to zero,

$$\lambda = \frac{-\left[6 + (9+\Theta)q_0Bo_{\mu\infty}\right]k^2 + \sqrt{\left[6 + (9+\Theta)q_0Bo_{\mu\infty}\right]^2k^4 + 8(k^2-k^4)Re}}{4Re}. \tag{B18}$$

https://doi.org/10.1017/jfm.2025.10933 Published online by Cambridge University Press

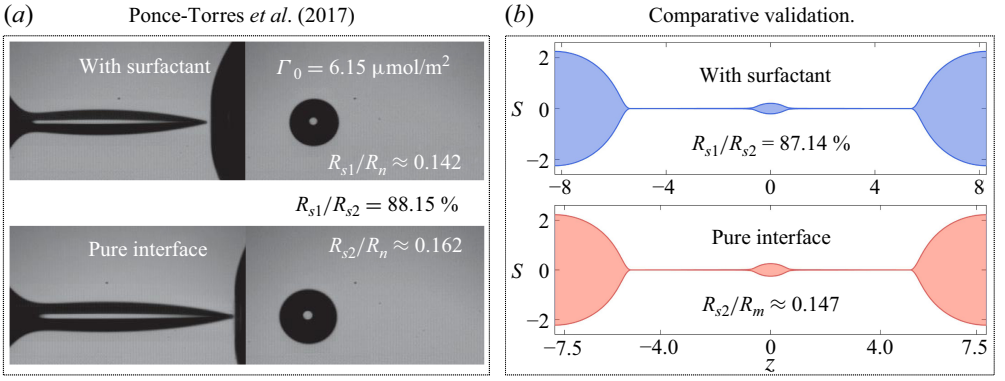


Figure 12. Comparison with the experimental results of Ponce-Torres *et al.* (2017) (reproduced with permission, American Physical Society), focusing on the reduction of satellite droplet size due to surfactants, considering surface viscosity.

Appendix C.

This section presents a detailed comparison with the experimental results of Ponce-Torres *et al.* (2017), which focused on the effects of surface viscosity on pendant liquid bridges and surfactant accumulation. Here, we primarily examine the variation in satellite droplet size. Since no electric field was present in the experiments, we disable electrostatic effects by setting the wall potential to $\phi_w = 0$ and the electrostatic Weber number to $Q = 0$. The surfactant concentration used in the experiments was $\Gamma_0 = 6.15\ \mu\text{mol m}^{-2}$, with negligible diffusion effects. Due to differences between the pendant bridge configuration in the experiments and the mathematical model used in this study, the comparison mainly focuses on the surfactant-induced suppression of satellite droplets. Based on the material properties reported in the literature, the surface dilational viscosity is $\kappa_s = 5.91 \times 10^{-8}\ (\text{kg m}^2)/(\mu\text{mol s}^{-1})$, and the surface shear viscosity is $\mu_s = 5.06 \times 10^{-8}\ (\text{kg m}^2)/(\mu\text{mol s})$. The corresponding dimensionless parameters are $Bo_{\kappa\infty} = \kappa_s \Gamma_0/(\mu R_n) = 0.187$ and $Bo_{\mu\infty} = \mu_s \Gamma_0/(\mu R_n) = 0.218$, where R_n denotes the radius of the experimental nozzle. Other selected parameters are $Pe_s = 10^4$ and $Re = 1$.

The experimental and numerical results are shown in figures 12(*a*) and 12(*b*), respectively. The presence of surfactants is observed to reduce the satellite droplet radius. Due to parameter discrepancies and model limitations, the ratio of the satellite droplet radius to the main droplet radius in the numerical results for a clean interface is $R_{s2}/R_m = 0.147$, whereas in the experiments, the corresponding ratio is $R_{s2}/R_n = 0.162$, exhibiting a notable difference of approximately 10 %. However, the ratio of satellite droplet sizes with and without surfactants, R_{s1}/R_{s2}, shows good agreement between experiments and simulations. This agreement supports the conclusion that increased surface viscosity suppresses satellite droplet formation, reinforcing the validity of both the present model and its predictions.

References

ANNA, S.L. 2016 Droplets and bubbles in microfluidic devices. *Annu. Rev. Fluid Mech.* **48** (2016), 285–309.

BAYGENTS, J.C. & SAVILLE, D.A. 1991 Electrophoresis of drops and bubbles. *J. Chem. Soc. Faraday Trans.* **87**, 1883–1898.

BORGES, R., CARMONA, M., COSTA, B. & DON, W.S. 2008 An improved weighted essentially non-oscillatory scheme for hyperbolic conservation laws. *J. Comput. Phys.* **227** (6), 3191–3211.

https://doi.org/10.1017/jfm.2025.10933 Published online by Cambridge University Press

BOUSSINESQ, M.J. 1913 Sur l'existence d'une viscosité seperficielle, dans la mince couche de transition séparant un liquide d'un autre fluide contigu. *J. Ann. Chim. Phys.* **29**, 349–357.
CAMPANA, D.M., UBAL, S., GIAVEDONI, M.D. & SAITA, F.A. 2011 A deeper insight into the dip coating process in the presence of insoluble surfactants: a numerical analysis. *Phys. Fluids* **23** (5), 052102.
CHAMPOUGNY, L., SCHEID, B., RESTAGNO, F., VERMANT, J. & RIO, E. 2015 Surfactant-induced rigidity of interfaces: a unified approach to free and dip-coated films. *Soft Matt.* **11**, 2758–2770.
CHEN, N., GAN, Y., LUO, Y. & JIANG, Z. 2022 A review on the technology development and fundamental research of electrospray combustion of liquid fuel at small-scale. *Fuel Process. Technol.* **234**, 107342.
CHENG, J.-B., LIU, Q.-Y., YANG, L.-J., REN, J.-X., TANG, H.-B., FU, Q.-F. & XIE, L. 2024 Pulsation mechanism of a Taylor cone under a single pulse voltage. *Phys. Rev. Fluids* **9**, 013701.
CHENG, J.-B., YANG, L.-J., FU, Q.-F., REN, J.-X., TANG, H.-B., SUN, D.-K. & SUN, X.-F. 2022 Pulsating modes of a Taylor cone under an unsteady electric field. *Phys. Fluids* **34** (1), 012007.
COLLINS, R.T., HARRIS, M.T. & BASARAN, O.A. 2007 Breakup of electrified jets. *J. Fluid Mech.* **588**, 75–129.
CONROY, D.T., CRASTER, R.V., MATAR, O.K. & PAPAGEORGIOU, D.T. 2010 Dynamics and stability of an annular electrolyte film. *J. Fluid Mech.* **656**, 481–506.
CONROY, D.T., MATAR, O.K., CRASTER, R.V. & PAPAGEORGIOU, D.T. 2011 Breakup of an electrified viscous thread with charged surfactants. *Phys. Fluids* **23** (2), 022103.
CRASTER, R.V., MATAR, O.K. & PAPAGEORGIOU, D.T. 2002 Pinchoff and satellite formation in surfactant covered viscous threads. *Phys. Fluids* **14** (4), 1364–1376.
CRASTER, R.V., MATAR, O.K. & PAPAGEORGIOU, D.T. 2009 Breakup of surfactant-laden jets above the critical micelle concentration. *J. Fluid Mech.* **629**, 195–219.
DATWANI, S.S. & STEBE, K.J. 1999 The dynamic adsorption of charged amphiphiles: the evolution of the surface concentration, surface potential, and surface tension. *J. Colloid Interface Sci.* **219** (2), 282–297.
DRAVID, V., SONGSERMPONG, S., XUE, Z., CORVALAN, C.M. & SOJKA, P.E. 2006 Two-dimensional modeling of the effects of insoluble surfactant on the breakup of a liquid filament. *Chem. Engng Sci.* **61**, 3577–3585.
EGGERS, J. & VILLERMAUX, E. 2008 Physics of liquid jets. *Rep. Prog. Phys.* **71** (3), 036601.
EGGERS, J.G. 1997 Nonlinear dynamics and breakup of free-surface flows. *Rev. Mod. Phys.* **69**, 865–930.
ELFRING, G.J., LEAL, L.G. & SQUIRES, T.M. 2016 Surface viscosity and Marangoni stresses at surfactant laden interfaces. *J. Fluid Mech.* **792**, 712–739.
FAUVEL, M., TRYBALA, A., TSELUIKO, D., STAROV, V.M. & BANDULASENA, H.C.H. 2022 Stability of two-dimensional liquid foams under externally applied electric fields. *Langmuir* **38** (20), 6305–6321.
GALLARDO, B.S., GUPTA, V.K., EAGERTON, F.D., JONG, L.I., CRAIG, V.S., SHAH, R.R. & ABBOTT, N.L. 1999 Electrochemical principles for active control of liquids on submillimeter scales. *Science* **283** (5398), 57–60.
HAMEED, M. & MALDARELLI, C. 2016 Effect of surfactant on the break-up of a liquid thread: modeling, computations and experiments. *Intl J. Heat Mass Transfer* **92**, 303–311.
HAMEED, M., SIEGEL, M., YOUNG, Y.-N., LI, J., BOOTY, M.R. & PAPAGEORGIOU, D.T. 2008 Influence of insoluble surfactant on the deformation and breakup of a bubble or thread in a viscous fluid. *J. Fluid Mech.* **594**, 307–340.
HERRADA, M.A., PONCE-TORRES, A., RUBIO, M., EGGERS, J. & MONTANERO, J.M. 2022 Stability and tip streaming of a surfactant-loaded drop in an extensional flow. Influence of surface viscosity. *J. Fluid Mech.* **934**, A26.
HOHMAN, M.M., SHIN, M., RUTLEDGE, G. & BRENNER, M.P. 2001*a* Electrospinning and electrically forced jets. I. Stability theory. *Phys. Fluids* **13** (8), 2201–2220.
HOHMAN, M.M., SHIN, M., RUTLEDGE, G. & BRENNER, M.P. 2001*b* Electrospinning and electrically forced jets. II. Applications. *Phys. Fluids* **13** (8), 2221–2236.
HUEBNER, A.L. & CHU, H.N. 1971 Instability and breakup of charged liquid jets. *J. Fluid Mech.* **49** (2), 361–372.
ISMAIL, N.B., MAKSOUD, F.J., GHADDAR, N., GHALI, K.F. & TEHRANI-BAGHA, A.R. 2016 Simplified modeling of the electrospinning process from the stable jet region to the unstable region for predicting the final nanofiber diameter. *J. Appl. Polym. Sci.* **133** (43), 44112.
JOYE, J.L., HIRASAKI, G.J. & MILLER, C.A. 1994 Asymmetric drainage in foam films. *Langmuir* **10**, 3174–3179.
KAMAT, P.M., WAGONER, B.W., THETE, S.S. & BASARAN, O.A. 2018 Role of marangoni stress during breakup of surfactant-covered liquid threads: reduced rates of thinning and microthread cascades. *Phys. Rev. Fluids* **3**, 043602.
KAS-DANOUCHE, S.A., PAPAGEORGIOU, D.T. & SIEGEL, M. 2009 Nonlinear dynamics of core-annular film flows in the presence of surfactant. *J. Fluid Mech.* **626**, 415–448.

https://doi.org/10.1017/jfm.2025.10933 Published online by Cambridge University Press

LAKDAWALA, A.M., SHARMA, A.K. & THAOKAR, R.M. 2016 A dual grid level set method based study on similarity and difference between interface dynamics for surface tension and radial electric field induced jet breakup. *Chem. Engng Sci.* **148**, 238–255.

LI, F. & HE, D. 2023 Dynamics of a surfactant-laden viscoelastic thread in the presence of surface viscosity. *J. Fluid Mech.* **966**, A35.

LI, F., KE, S.-Y., YIN, X.-Y. & YIN, X.-Z. 2019 Effect of finite conductivity on the nonlinear behaviour of an electrically charged viscoelastic liquid jet. *J. Fluid Mech.* **874**, 5–37.

LÓPEZ-HERRERA, J.M., GAÑÁN-CALVO, A.M., POPINET, S. & HERRADA, M.A. 2015 Electrokinetic effects in the breakup of electrified jets: a volume-of-fluid numerical study. *Intl J. Multiphase Flow* **71**, 14–22.

LÓPEZ-HERRERA, J.M. & GAÑÁN-CALVO, A.M. 2004 A note on charged capillary jet breakup of conducting liquids: experimental validation of a viscous one-dimensional model. *J. Fluid Mech.* **501**, 303–326.

LÓPEZ-HERRERA, J.M., RIESCO-CHUECA, P. & GAÑÁN-CALVO, A.M. 2005 Linear stability analysis of axisymmetric perturbations in imperfectly conducting liquid jets. *Phys. Fluids* **17** (3), 034106.

MARTÍNEZ-CALVO, A. & SEVILLA, A. 2020 Universal thinning of liquid filaments under dominant surface forces. *Phys. Rev. Lett.* **125**, 114502.

MARTÍNEZ-CALVO, A., RIVERO-RODRÍGUEZ, J., SCHEID, B. & SEVILLA, A. 2020 Natural break-up and satellite formation regimes of surfactant-laden liquid threads. *J. Fluid Mech.* **883**, A35.

MARTÍNEZ-CALVO, A. & SEVILLA, A. 2018 Temporal stability of free liquid threads with surface viscoelasticity. *J. Fluid Mech.* **846**, 877–901.

MCGOUGH, P.T. & BASARAN, O.A. 2006 Repeated formation of fluid threads in breakup of a surfactant-covered jet. *Phys. Rev. Lett.* **96**, 054502.

MESTEL, A.J. 1996 Electrohydrodynamic stability of a highly viscous jet. *J. Fluid Mech.* **312**, 311–326.

MILLIKEN, W.J., STONE, H.A. & LEAL, L.G. 1993 The effect of surfactant on the transient motion of Newtonian drops. *Phys. Fluids A: Fluid Dyn.* **5** (1), 69–79.

MONTANERO, J.M. & GANAN-CALVO, A.M. 2020 Dripping, jetting and tip streaming. arXiv: 1909.02073.

NIE, Q., LI, F., MA, Q., FANG, H. & YIN, Z. 2021 Effects of charge relaxation on the electrohydrodynamic breakup of leaky-dielectric jets. *J. Fluid Mech.* **925**, A4.

OZAN, S.C. & JAKOBSEN, H.A. 2019 On the role of the surface rheology in film drainage between fluid particles. *Intl J. Multiphase Flow* **120**, 103103.

PAPAGEORGIU, D.T. 2002 *Hydrodynamics of Surface Tension Dominated Flows*, pp. 41–88. Springer Vienna.

PONCE-TORRES, A., HERRADA, M.A., MONTANERO, J.M. & VEGA, J.M. 2016*a* Linear and nonlinear dynamics of an insoluble surfactant-laden liquid bridge. *Phys. Fluids* **28** (11), 112103.

PONCE-TORRES, A., MONTANERO, J.M., HERRADA, M.A., VEGA, E.J. & VEGA, J.M. 2017 Influence of the surface viscosity on the breakup of a surfactant-laden drop. *Phys. Rev. Lett.* **118**, 024501.

PONCE-TORRES, A., RUBIO, M., HERRADA, M.A., EGGERS, J. & MONTANERO, J.M. 2020 Influence of the surface viscous stress on the pinch-off of free surfaces loaded with nearly-inviscid surfactants. *Sci. Rep. UK* **10**, 16065.

PONCE-TORRES, A., VEGA, E.J. & MONTANERO, J.M. 2016*b* Effects of surface-active impurities on the liquid bridge dynamics. *Exp. Fluids* **57**, 1–12.

PROSSER, A.J. & FRANSES, E.I. 2001 Adsorption and surface tension of ionic surfactants at the air-water interface: review and evaluation of equilibrium models. *Colloids Surf. A: Physicochem. Engng Aspects* **178**, 1–40.

QUÉRÉ, D., DE RYCK, A. 1998 Le mouillage dynamique des fibres. *Ann. Phys. PARIS* **23**, 1–149.

RAYLEIGH, L. 1878 On the instability of jets. *Proc. Lond. Math. Soc.* **s1-10** (1), 4–13.

RENEKER, D.H., YARIN, A.L., FONG, H. & KOOMBHONGSE, S. 2000 Bending instability of electrically charged liquid jets of polymer solutions in electrospinning. *J. Appl. Phys.* **87** (9), 4531–4547.

RODRÍGUEZ-RODRÍGUEZ, J., SEVILLA, A., MARTÍNEZ-BAZÁN, C. & GORDILLO, J.M. 2015 Generation of microbubbles with applications to industry and medicine. *Annu. Rev. Fluid Mech.* **47** (2015), 405–429.

SAVILLE, D.A. 1971*a* Electrohydrodynamic stability: effects of charge relaxation at the interface of a liquid jet. *J. Fluid Mech.* **48** (4), 815–827.

SAVILLE, D.A. 1971*b* Stability of electrically charged viscous cylinders. *Phys. Fluids* **14** (6), 1095–1099.

SAVILLE, D.A. 1997 Electrohydrodynamics: the Taylor–Melcher leaky dielectric model. *Annu. Rev. Fluid Mech.* **29** (1997), 27–64.

SCHEID, B., DELACOTTE, J., DOLLET, B., RIO, E., RESTAGNO, F., VAN NIEROP, E.A., CANTAT, I., LANGEVIN, D. & STONE, H.A. 2010 The role of surface rheology in liquid film formation. *Europhys. Lett.* **90** (2), 24002.

SCHEID, B., DORBOLO, S., ARRIAGA, L.R. & RIO, E. 2012 Antibubble dynamics: the drainage of an air film with viscous interfaces. *Phys. Rev. Lett.* **109**, 264502.

https://doi.org/10.1017/jfm.2025.10933 Published online by Cambridge University Press

SCRIVEN, L.EDWARD & STERNLING, C.V. 1960 The marangoni effects. *Nature* **187**, 186–188.
SEIWERT, J., DOLLET, B. & CANTAT, I. 2014 Theoretical study of the generation of soap films: role of interfacial visco-elasticity. *J. Fluid Mech.* **739**, 124–142.
STONE, H.A. & LEAL, L.G. 1990 The effects of surfactants on drop deformation and breakup. *J. Fluid Mech.* **220**, 161–186.
SWEET, R.G. 1965 High frequency recording with electrostatically deflected ink jets. *Rev. Sci. Instrum.* **36** (2), 131–136.
TIMMERMANS, M.-L.E. & LISTER, J.R. 2002 The effect of surfactant on the stability of a liquid thread. *J. Fluid Mech.* **459**, 289–306.
WANG, Q. 2012 Breakup of a poorly conducting liquid thread subject to a radial electric field at zero Reynolds number. *Phys. Fluids* **24** (10), 102102.
WANG, Q., MÄHLMANN, S. & PAPAGEORGIOU, D.T. 2009 Dynamics of liquid jets and threads under the action of radial electric fields: microthread formation and touchdown singularities. *Phys. Fluids* **21** (3), 032109.
WANG, Q. & PAPAGEORGIOU, D.T. 2011 Dynamics of a viscous thread surrounded by another viscous fluid in a cylindrical tube under the action of a radial electric field: breakup and touchdown singularities. *J. Fluid Mech.* **683**, 27–56.
WANG, Y., HASHIMOTO, T., LI, C.-C., LI, Y.-C. & WANG, C. 2018 Extension rate of the straight jet in electrospinning of poly(n-isopropyl acrylamide) solutions in dimethylformamide: influences of flow rate and applied voltage. *J. Polym. Sci. B: Polym. Phys.* **56** (4), 319–329.
WEE, H., WAGONER, B.W. & BASARAN, O.A. 2022 Absence of scaling transitions in breakup of liquid jets caused by surface viscosity. *Phys. Rev. Fluids* **7**, 074001.
WEE, H., WAGONER, B.W., GARG, V., KAMAT, P.M. & BASARAN, O.A. 2021 Pinch-off of a surfactant-covered jet. *J. Fluid Mech.* **908**, A38.
WEE, H., WAGONER, B.W., KAMAT, P.M. & BASARAN, O.A. 2020 Effects of surface viscosity on breakup of viscous threads. *Phys. Rev. Lett.* **124**, 204501.
WODLEI, F., SEBILLEAU, J., MAGNAUDET, J. & PIMIENTA, V. 2018 Marangoni-driven flower-like patterning of an evaporating drop spreading on a liquid substrate. *Nat. Commun.* **9**, 820.
YAO, M., YANG, L. & FU, Q. 2021 Temporal instability of surfactant-laden compound jets with surface viscoelasticity. *Eur. J. Mech. B/Fluids* **89**, 191–202.

https://doi.org/10.1017/jfm.2025.10933 Published online by Cambridge University Press